UNIVERSITY OF OKLAHOMA

GRADUATE COLLEGE

INVESTIGATIONS INTO SELECTIVE LASER MELTING OF SILICON CARBIDE-SILICON DIOXIDE CERAMIC COMPOSITES

A THESIS

SUBMITTED TO THE GRADUATE FACULTY

in partial fulfillment of the requirements for the

Degree of

MASTER OF SCIENCE

By

SEAN BROWNLEE

Norman, Oklahoma

2024

INVESTIGATIONS INTO SELECTIVE LASER MELTING OF SILICON CARBIDE-SILICON DIOXIDE CERAMIC COMPOSITES

A THESIS APPROVED FOR THE

SCHOOL OF AEROSPACE AND MECHANICAL ENGINEERING

BY THE COMMITTEEE CONSISTING OF

Dr. Yingtao Liu, Chair

Dr. Chris Billings, Co-Chair

Dr. Jivtesh Garg

Acknowledgements

I must first extend my gratitude to Dr. Yingtao Liu for his continual support of the SMIS Lab and his students. Dr. Liu gave generously of his time, wisdom, and funds in support of this project.

I would like to thank my excellent instructors from primary school to post-grad for their unwavering dedication and support throughout my educational journey.

I must formally acknowledge and extend gratitude for the previous work of the 2020, 2021, and 2022 capstone teams for development of the machine's chassis. Although I have modified many aspects of the control schema, the chassis remains as previously designed and is in good condition after much use.

I would also like to thank Kevin O'Connor, his team, and the open-source community for their development of and tireless work on the Klipper software suite. Their contribution makes interfacing with these rapidly evolving systems possible.

Among other faculty members, I'm grateful to Dr. Billings for providing technical and professional advice as I began to navigate the field of additive manufacturing and postgraduate education.

I would like to thank my friends for their understanding and comradery. We've shared many rough roads together.

Thank you to my girlfriend, Rebecca, for energizing my spirit and ensuring that I always stumble uphill.

Last, but certainly not least, I would like to thank my family for always supporting my endeavors and convincing me that I have value to share with the world.

Table of Contents

Table of Figures

Table of Tables

Abstract

This investigative thesis explores the potential of leveraging Selective Laser Melting (SLM) with silicon-based ceramic substrates to form three-dimensional silicon-based glass-ceramic composite parts. A Selective Laser Processing (SLP) machine was developed to conduct experimental research. The machine was utilized to study the effects of silicon dioxide (SiO_2) additive in silicon carbide (SiC) substrates as well as the effect of Scanning Energy (SED) on resulting fabricated line widths and fabricated line uniformity. Preliminary and experimental fabricated line width prediction models as functions of SED, substrate SiC content, and scale of SiO_2 particulate additive in the substrate were created. The machine was also utilized to study the effects of SED and scanning strategy on defect formation in fabricated square specimens.

It was found that by SLM, melt pool formation and melt pool solidification occurred in substrates containing primarily SiC. Additionally, successful bonding of joints, common in SLM of three-dimensional components, was demonstrated. The exact chemical composition of the final fabricated specimens remained unclear; however, some evidence pointed to the subversion of sublimation of SiC in standard atmosphere under rapid heating and cooling cycles.

The results provide a platform for future investigations in SLM of SiC and can be used as an impetus for increasing efforts to account for and control the process parameters involved. It is expected that with increased experimental, theoretical, and numerical modeling, as well as increased control of process parameters, the fabrication of three-dimensional components by SLM is possible using SiC substrates.

Chapter 1: Introduction

1.1 Overview of Silicon Dioxide, Silicon Carbide and their Composites

Silicon-based ceramics are increasingly finding diverse applications across industries ranging from aerospace to electronics. The performance of these materials is driving demand for new manufacturing processes [1]. Silicon carbide (SiC) and silicon dioxide (SiO_2) represent two prominent types of these ceramics.

Within the 21st century, SiC has become one of the most commercially significant advanced ceramics in industrial applications in the world today, only surpassed by Al_2O_3 in market impact [2]. SiC is known for having higher hardness than sapphire, a chemical inertness similar to graphite, thermal conductivity similar to iron, refractory strength 50-200% higher than Al_2O_3, and superior electrical semiconductive properties over pure silicon. It is also known for its low coefficient of thermal expansion [2]. It has been well-recognized that SiC is one of the lightest, hardest, and strongest technical ceramics and has greater than the average toughness of the brittle ceramics. [3] The outstanding properties of SiC make it ideal for high-temperature and physical wear applications [4]. These applications include gas turbine engines, MOSFET devices, abrasives, cutting tools, ballistic armor, and nuclear fuel cladding [2,5].

Silicon dioxide, bound as silicates in nature, is the most abundant material on Earth's surface as it makes up ca. 75% of Earth's Crust by weight [6]. Crystalline silica products are known for their high thermal stability, electrical insulation, optical transparency, chemical inertness, hardness, abundance, and biocompatibility. SiO_2 is also known for its low thermal expansion coefficient and low density. SiO_2 is found in concrete, electronics, optics, refractories, coatings, insulation, and many composites [7].

The complementary properties of SiC and SiO_2 have generated interest in the development of SiC/SiO_2 composite ceramics. This interest stems from the potential to leverage the mechanical strength of SiC and the high thermal shock resistance of SiO_2, resulting in a more robust composite material with high thermal stability, corrosion resistance, strength, and resistance to thermal shock [2]. In the 1990s, a study explored the effect of reinforcing fused silica with SiC fibers. Their findings demonstrated that the tensile strength of the SiC-SiO_2 composite was up to four times greater than that of bulk fused SiO_2, which highlighted a significant improvement in mechanical properties afforded by these composites [8]. Further advancements were made by Lee et al., who performed extensive structural and microstructural studies on the use of SiO_2 as a sintering aid in the SiC part fabrication process, which results in a SiC-SiO_2 glass-ceramic composite. Their research revealed that the addition of SiO_2 in sintered SiC substrates increased the compressive strength samples by a factor of six over pure SiC substrates [9]. Another study conducted by Li et al. found improved antioxidative and mechanical properties in Carbon-Carbon composites via the application of a SiO_2-SiC surface layer [10]. These findings underscore the synergistic benefits of combining SiC and SiO_2 to form composite ceramics. Consequently, SiC-SiO_2 composites are poised to offer superior performance in demanding applications, such as high-temperature structural components.

These studies paved the way for further exploration into optimizing the ratios and processing methods for SiC-SiO_2 composites. The continued research and development in this area holds promise for fabrication of components using materials that can withstand extreme conditions.

1.2 Types of Silicon Carbide and Silicon Dioxide

Silicon carbide is similar in crystallographic structure to carbon and contains 88% covalency in its atomic bonds. SiC is capable of polytypism, and many crystalline polytypes exist. Over 150

polytypes of SiC have been discovered. It is commonly found in cubic, hexagonal, and rhombohedral lattices. [11]. Industrially relevant polytypes include α-SiC and β-SiC. Phase transformation of these polytypes occurs at temperatures around 2000°C. The standard industrial form of SiC is α-SiC, which includes 2H, 4H, 6H, and 15R and is formed primarily by the Acheson process. The reason for the commonality of these polytypes is not yet well understood [2]. Single crystal SiC components are common in the electronics industry, and Hot Pressed SiC (HPSC) is the most common polycrystalline SiC in all other industries due to its high fabricated density relative to its theoretical density. The theoretical properties of SiC are closely approximated by HPSC [2].

Silicon dioxide exists in a remarkable number of forms, such as: crystalline, amorphous, colloidal, hydrated, aerogel, and micro silica [7]. The most common and thermodynamically stable crystallographic form is quartz. Variations in quartz include low quartz (α-quartz) and high quartz (β-quartz) with phase transitions occurring at elevated temperatures. Other significant crystalline forms of SiO_2 include cristobalite and tridymite, each with complex sequences of phase transitions occurring at various thermal cycles. Many of these diverse forms of SiO_2 are paramount in industrial applications from electronics and optical devices to high-temperature ceramics and abrasives [6].

A few select types of SiC-SiO_2 composites have been investigated. Fiber reinforced composites in the form of SiC Fiber-Reinforced SiO_2 have been studied to improve the toughness and thermal stability of bulk SiO_2 boules [8]. Particulate composites incorporating SiC particles in SiO_2 matrices and vice versa have been implemented to investigate maximization of abrasion resistance and refractory strength. Also, SiC and SiO_2 have been sintered and melted in concert to form glass-ceramic composites of higher density than that of pure substrates of these materials fabricated

independently. These composites have also exhibited blended characteristics of the two materials [9].

1.3 Thesis Outline

The primary goal of this work was to experimentally assess the efficacy of fabricating silicon-based glass-ceramics and their composites by SLM of blended particulate substrates. The goal was achieved through characterization and quantification of the geometrical properties of fabricated samples.

The primary reason for this investigation was the apparent discovery of the capability of subversion of the sublimation of SiC through rapid photothermal heating of the substrate, applied by a diode laser. This subversion appeared to allow and promote the formation of short-lived SiC melt pools in atmospheric conditions. This phenomenon pairs well with the SLM process because these short-lived melt pools can be used to additively fabricate parts of complex geometries.

The effect of SiO_2 particulate additions in SiC substrates and varied SED (SED) on fabricated line widths and their uniformity were studied to lay the groundwork for future additive manufacturing of complex three-dimensional components composed of SiC-SiO_2 glass-ceramic composites. The preliminary models created to predict these effects provide a platform for future experimentation. The measured properties also allude to characterization of the SLM melt pool size, stability, and controllability in these substrates and environmental conditions.

The hypothesis was stated as follows:

If process parameters and environmental conditions are controlled and optimized, then it is possible to fabricate SiC-SiO_2 composite ceramic components by SLM because precise control of the laser, atmosphere, substrate, and powder feedstock can effectively manage the thermal

dynamics and chemical reactions necessary for achieving a homogenous melt pool and subsequent solidification, ensuring the desired microstructure and material properties of the fabricated component.

The investigation of this hypothesis was performed experimentally. This process began with conducting literature review of SiC, SiO_2, their composites, and their manufacturing processes (Chapter 2). Next, a machine was developed to perform powder bed additive manufacturing (Chapter 3). The machine was then modified to perform powder bed selective laser processing (Chapter 3). Figure 1, below, shows an image of the machine developed.

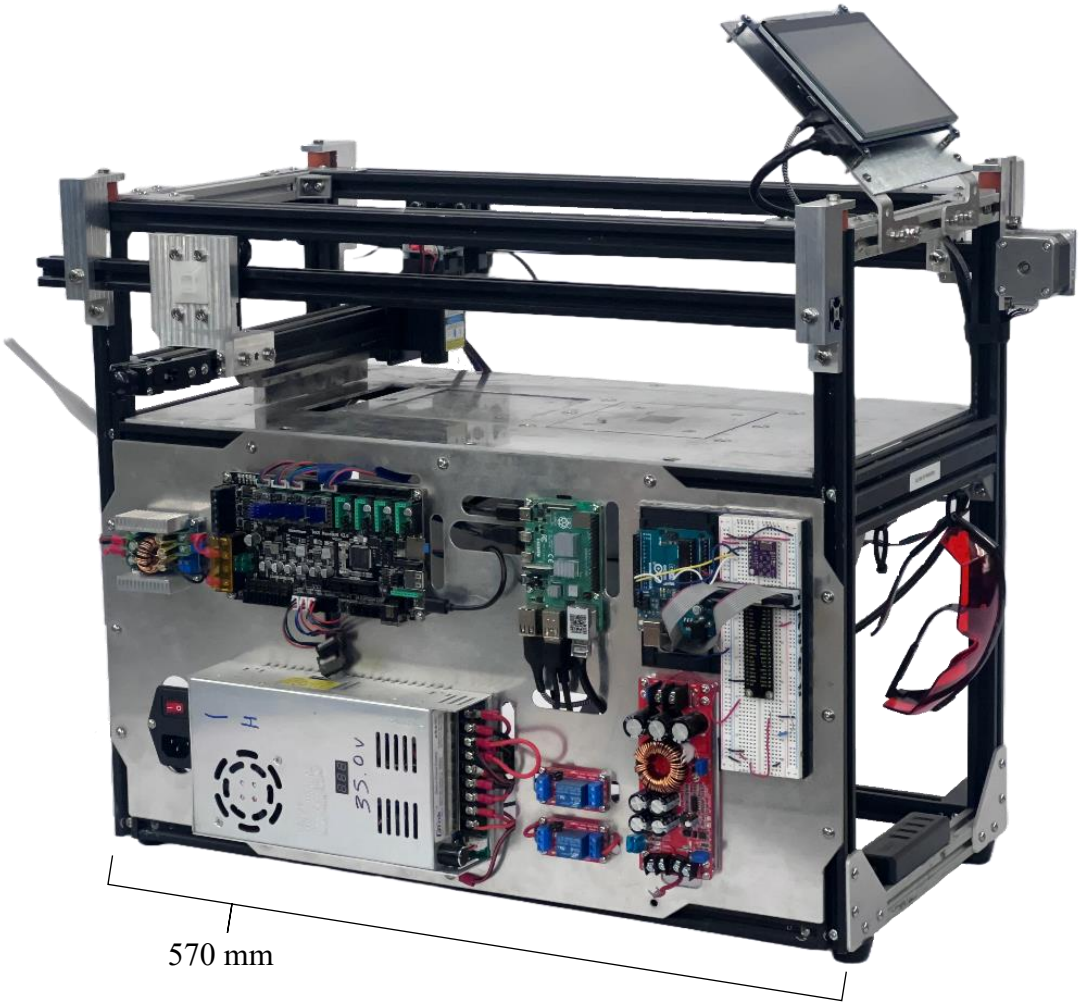

Figure 1: Image of Machine Developed for SLM

The machine was operated to fabricate samples (Chapter 4). Optical microscopy and image processing techniques were leveraged to characterize the effect of certain process parameters on the resulting geometry of fabricated samples (Chapter 4).

It was found that, even with preliminary efforts to control melt pool stability, bed adhesion, SED, vibration damping, machine rigidity, substrate purity, and environmental conditions, SLM of SiC/SiO_2 substrates is a viable manufacturing technique.

With proper control of the process parameters, it is possible to additively manufacture, by SLM, SiC/SiO_2 glass-ceramic components with the potential for having high refractory strength, thermal shock resistance, and chemical stability at high temperatures.

Chapter 2: Literature Review

2.1 Conventional Manufacturing of Silicon Carbide and Silicon Dioxide Parts

The first recorded use of SiC was by Berzelius in 1824 [12] In 1892 Acheson invented the first industrial process for the synthesis of SiC [13]. SiC has now been an industrial product for over a century [5].

The conventional manufacturing of SiC and SiO_2 parts involves various techniques, each according to the component's intended application. SiC is commonly manufactured by melt casting, pressureless sintering, hot pressing, hot isostatic pressing, and chemical vapor deposition [5].

The manufacture of SiC components remains difficult because it is a covalent ceramic which can decompose and sublimate above temperatures of 2545°C forming liquid silicon and carbon [14]. Therefore, it is difficult to create large molten or formable masses of SiC.

SiO_2 differs from SiC in the sense that it occurs much more prevalently in nature [6]. Because of this, SiO_2 primarily is mined, instead of synthesized, in the form of quartz. It has been used as an industrial material since the dawn of the industrial revolution [15]. Nearly all demand for pure quartz crystal for the electronic industry is, however, met with synthesized quartz produced using the hydrothermal process [6].

Silicon-based glass-ceramic composites are synthesized by methods similar to those found in the synthesis of SiC. These synthesized materials can generally be prepared in bulk with these modern techniques; however, the forming of these ceramics into useful component geometries remains the work of subtractive manufacturing processes which are, primarily, grinding and, secondarily, milling in rare cases [16,17]. These subtractive fabrication processes are inherently limited to the

production of simple part geometries. These methods cannot readily produce internal geometries such as microchannels for part cooling or functionally graded materials that often find utility in extreme wear and high temperature applications such as in turbomachinery or in combustion chambers.

2.2 Review of Additive Manufacturing

Traditional manufacturing methods of silicon-based ceramics often face significant limitations such as higher production costs, lengthier processing times, and difficulty in achieving complex geometries as opposed to metal matrix materials. These limitations hinder the potential for broader application of ceramics in numerous technological fields, and they provide an impetus to search for new manufacturing methods.

Additive manufacturing was developed in the early 1980s as a fabrication technology that aims to manufacture three-dimensional objects by adding or bonding material in a layer-by-layer approach. Material is generally joined, solidified, or deposited by computer numerical control. This technology provides a new set of manufacturing capabilities that extend beyond the limitations of conventional processes. The primary benefits of this technology are the elimination of part-specific tooling, increased geometric complexity, reduced waste, shorter lead times, and energy efficiency. This technology is rapidly developing and gaining popularity in commercial and consumer markets [18].

Additive manufacturing is delineated into several distinct processes, each with their own combination of material deposition mechanism, material bonding mechanism, and range of applicable materials. Machines that carry out the additive manufacturing process are also known as 3D printers. Common 3D printers on the market today utilize a method called Fused Deposition

Modeling (FDM) and are generally limited to low-strength thermoplastics such as Polylactic Acid (PLA) and Acrylonitrile Butadiene (ABS). Other additive manufacturing processes include Stereolithography (SLA), Digital Light Processing (DLP), Direct Ink Writing (DIW), Electron Beam Melting (EBM), Multijet Fusion (MJF), Binder Jetting, Directed Energy Deposition (DED), Laminated Object Manufacturing (LOM), Cold Metal Fusion (CMF), Continuous Liquid Interface Production (CLIP), Selective Laser Sintering (SLS), and Selective Laser Melting (SLM) [18].

A vast majority of the machines developed for additive manufacturing are Powder Bed Selective Laser Processing (PBSLP) machines. These machines commonly consist of four essential parts. These parts are the laser, the powder supply, the build platform, and the powder spreader/recoater. Each of these machines utilize a layer-by-layer build process in the gravity down configuration. Machines equipped with a rolling drum recoater are capable of in situ powder compaction of the substrate [19].

A machine was in development to perform Binder Jetting Additive Manufacturing (BJAM) at the University of Oklahoma. The machine was modified to perform SLS and SLM.

In the SLS process, a laser selectively scans each layer of powder. In this process, the energy absorbed by the powder increases the temperature of the particles enough to partially fuse and bond contiguous particles together. Often, binders and additives are used to assist in the binding process. After the part has been fabricated in this manner, it generally must undergo further post processing procedures. Bed adhesion is not generally required for the first layer because thermally induced stresses and warping phenomena are negligible [20].

The steps of the SLS process are as follows:

1. Powder Preparation: Powder is mixed and deposited into the powder supply

2. Powder Spreading: A layer of powder material is spread in a thin and even manner across the build platform using the recoating mechanism forming the build substrate
3. Laser Scanning: A laser beam is directed to thermally energize the substrate to bond the loose particulate in a selective manner
4. Layer Building: Once a layer is complete, the build platform lowers, and a new layer of powder is applied on top of the previous layer, and binding of the new layer begins.
5. Curing: The part, or each layer, is hardened or stabilized using thermal or photoreactive processes
6. Depowdering: The unbonded, loose powder is removed and is prepared for recycle
7. Post-Processing: The part is further processed by sintering, infiltration, and/or finishing

The SLM process is very similar to the SLS process, however, more energy is absorbed by the substrate, such to momentarily liquefy the powder and form a melt pool. In this way, SLM is a combination of laser welding and SLS. The fabrication procedure of SLM is similar to that of SLS; however, after scanning, the parts require different post-processing steps, such as heat-treating for stress relief or reformation of the microstructure. Additionally, the SLM process generally introduces a high degree of complexity over SLS processes because of phenomena introduced by melt pool formation and an expanded heat-affected zone [21].

SLS, and SLM machines have remained out-of-reach for the average consumer due to the lowest unit cost being on the order of ten thousand dollars on the low end, but they are rapidly increasing presence in industry as technology develops [22].

One process parameter of interest in SLS and SLM techniques is the SED (SED) [23]. The SED can be calculated as follows:

$$q = \frac{W}{H \cdot v_{scan}} \quad \text{Eq. 1}$$

where q represents the laser energy density in J/mm^2, W is laser power in watts, H is the laser focal diameter in mm, and v is the scanning velocity in mm/s. The formula in Eq. 1 is generalized for one-dimensional scanning. The formula can be extended to compute energy density in two-dimensional, layer scanning as follows:

$$q = \frac{W}{H \cdot v_{scan} \cdot H_s} \quad \text{Eq. 2}$$

where H_s represents the hatch spacing of the scan strategy in mm. This is the distance between the centerlines of parallel scanning paths. Studies have been conducted on the direct effect that variations of SED have on densification, microstructure, and mechanical properties in various material substrates. The research highlights the importance of a well-developed understanding of the substrate response to variations in the SED [24–26].

2.3 Review of Powder Bed Selective Laser Processing of Silicon-Based Ceramics

Research in powder bed selective laser processing of ceramics began in 1992 and interest has grown exponentially since then [19]. Indirect and direct methods of PBSLP of ceramics delineates techniques which, respectively, do and do not incorporate the use of a sacrificial polymer binder additive in the substrate to assist with bonding. However, there are exceptions to this rule in the case of additions of binders or precursors in the substrate that remain within the fabricated part after all processing is complete [19].

Process parameters and scanning strategies remain the focus of efforts to optimize the quality of fabricated components. A diagram of some of the parameters involved in substrate selection that

have been found to influence the build process and the fabricated part density, relative to the theoretical density of the substrate, is presented in Figure 2 below.

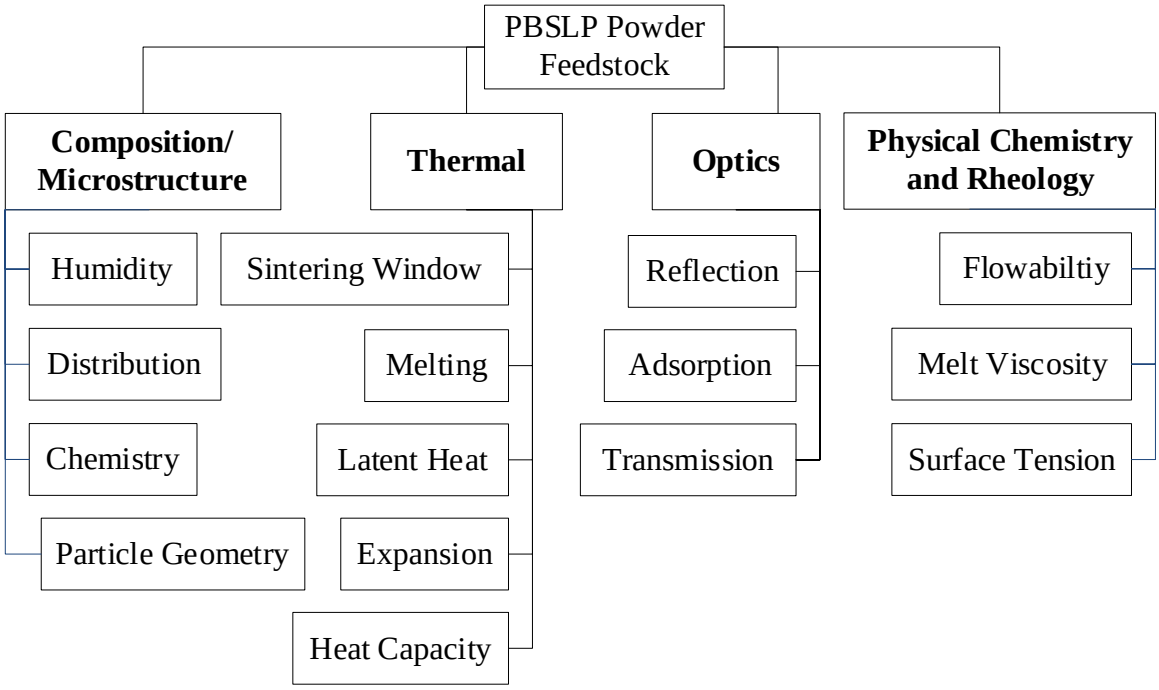

Figure 2: Diagram of Influencing Parameters for PBSLP Powders

The diagram of Figure 2 shows the number of factors to consider and degrees of freedom in the optimization problem of powder selection. After a ceramic feedstock has been selected, the work of accounting for these factors by optimization of the process parameters begins.

In three-dimensional part fabrication, the Volumetric SED (VSED) has been found to directly affect densification, mechanical properties, defects, and microstructure. The formula to compute the VSED parameter is an extension of the SED formula presented in Eq. 2, extended to account for the thickness of each layer [27]. It is worth noting that the volumetric energy density does not account for the kinetics of irradiated materials to describe mass and heat transfer between the laser path and the surrounding substrate.

SiC parts have been additively fabricated in labs, and their material properties are promising. For example, direct SLS of SiC in the absence of binders, additives, or other initial powder mixtures was experimentally investigated with a numerical approach to process parameter optimization. The study incorporated spark plasma sintering as a post-processing treatment to fabricate SiC samples of up to 96% relative density [28]. There was also an effort by Meyers et al. to utilize Si as a melting agent to bind the SiC particles by SLS, impregnate the preforms with phenolic resin, perform pyrolysis on the preforms to yield porous carbon and subject them to Si infiltration. This process successfully formed fully dense parts with 84 vol% composition of SiC [29,30].

The current consensus in the literature is that direct SLM of SiC substrates is impossible due to SiC lacking a melt phase under normal atmospheric conditions, as it decomposes at 2,545°C [19,31]. However, this decomposition certainly does not occur instantaneously; therefore, it may be possible to form a short-lived melt pool that cools and resolidifies before a vast majority of the decomposition takes place. This subversion of sublimation would allow for SLM of SiC substrates.

It is also possible that the inclusion of additives to form an eutectic substrate could promote melt pool formation in SiC substrates. In this case, silicon-based glass-ceramic composites of high relative density could be fabricated by direct SLM.

2.4 Previous Work: Early Stages Development of a Binder Jetting Ceramic 3D Printer

The machine that was modified and used to conduct the research presented in this work entered the design phase as a capstone project in 2020. The project's objective was to create a 3D printer for researching BJAM of ceramics. Development of the machine was continued by capstone teams in 2021 and 2022.

The frame and powder beds of the machine were developed and constructed by the 2020 and 2021 capstone teams. A worm drive gantry system was added to the frame during this time. The control electronics were not within scope at this stage of development.

The 2022 capstone team replaced the gantry system, electronics hardware, and software for control of the machine. The gantry system, implemented in 2022, is a belt-drive, cartesian system. This system increased the gantry speed and precision. The state of the frame and gantry system as received from the 2022 capstone team is shown in Figure 3 below.

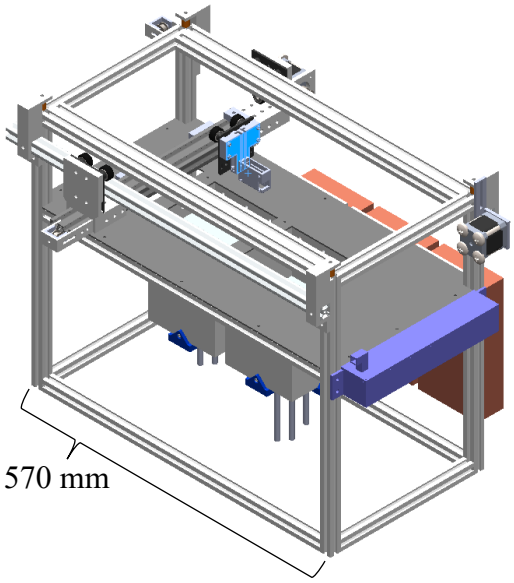

Figure 3: Digital Render of the Machine Assembly as Received from Previous Work

The chassis was exceptionally square and did not require any immediate modification. The electrical signals for machine control were handled by the general-purpose input-output pins of a Raspberry Pi single board, general purpose computer. The wiring harness and electrical components were in the breadboard prototyping stage of development. The electronic system allowed for open loop control of the gantry system. It also implemented a serial protocol interface intended for communication with and control of the inkjet print-head, however a GCODE system was not yet implemented.

At this stage, the printer control commands had to share CPU scheduling with the operating system and other services running on the Raspberry Pi. Therefore, the machine was not a real time system. This architecture was not capable of complex motor control and micro-stepping of the stepper motors.

Also, at this stage, the high-frequency print-head control signals arrived at the print head in a scrambled state after undergoing a logic level shifting process. Solving this problem was listed as the primary recommendation for future work in the 2022 Capstone Team's final report.

The frame, powder bed systems, and gantry system from this phase of development remain fully functional and unmodified after the modifications made to the machine that were implemented in 2023 and 2024.

Chapter 3: Methodology

3.1 Conversion to Klipper Control Schema and GCODE Interface

To mature the machine developed in previous work into a powder bed additive manufacturing machine, the lower-level control and interfacing of print-head and print bed translation was first abstracted to a standardized interface. GCODE systems have become the standard for computer numerical control. The machine was upgraded to this standard of control by integration of the popular, open source Klipper software suite.

Klipper is a 3D-Printer firmware. It combines the power of a general-purpose computer with one or more micro-controllers [32]. It allows for seamless, GCODE based, control of 3D printers. Adoption of this firmware and accompanying software for control of this printer was a necessary step towards productively interfacing with the machine. The Klipper source code can be found at https://github.com/Klipper3d/klipper.git

Klipper, running on the microcontroller, works by dispatching commands to the printer hardware, which are received from a host computer running a service called Klippy. Klippy performs calculations for printer control and transmits resulting low-level commands to Klipper based on inputs received from a Unix Domain Socket. The Unix Domain Socket receives messages by HTTP protocol received from a web server. There are multiple, open source, web server interfaces available for Klipper. For this system Mainsail was selected for this system because it is easy to install on a Raspberry Pi. It comes on a prepackaged Raspberry Pi operating system called an image.

When the Raspberry Pi is powered on, the Klippy software initializes using a configuration file that specifies the hardware configuration of the machine and adds any modules necessary for

machine operation. This system is useful in the realm of custom 3D printing machines that may implement a range of microcontrollers, sensors, motors, motor drivers, cooling systems, heating systems, screens, and I/O devices. All these systems can be controlled by Klipper, but Klipper/Klippy may require software modification for integration with unique hardware. An

3.2 Development of Electronics System

The electronics system of the machine was redesigned for implementation of the Klipper software suite. A mounting plate was designed for the machine to organize the electronics and increase reliability by decreasing the probability of erroneous shorts and disconnections of wiring. This was achieved through careful selection of pass-through points that allowed for containment of loose wiring within the frame and body of the machine. A diagram of the electronics system, fixed to the mounting plate, that was developed for conversion to the Klipper software suite and for integrating print-head control is shown in Figure 4 below.

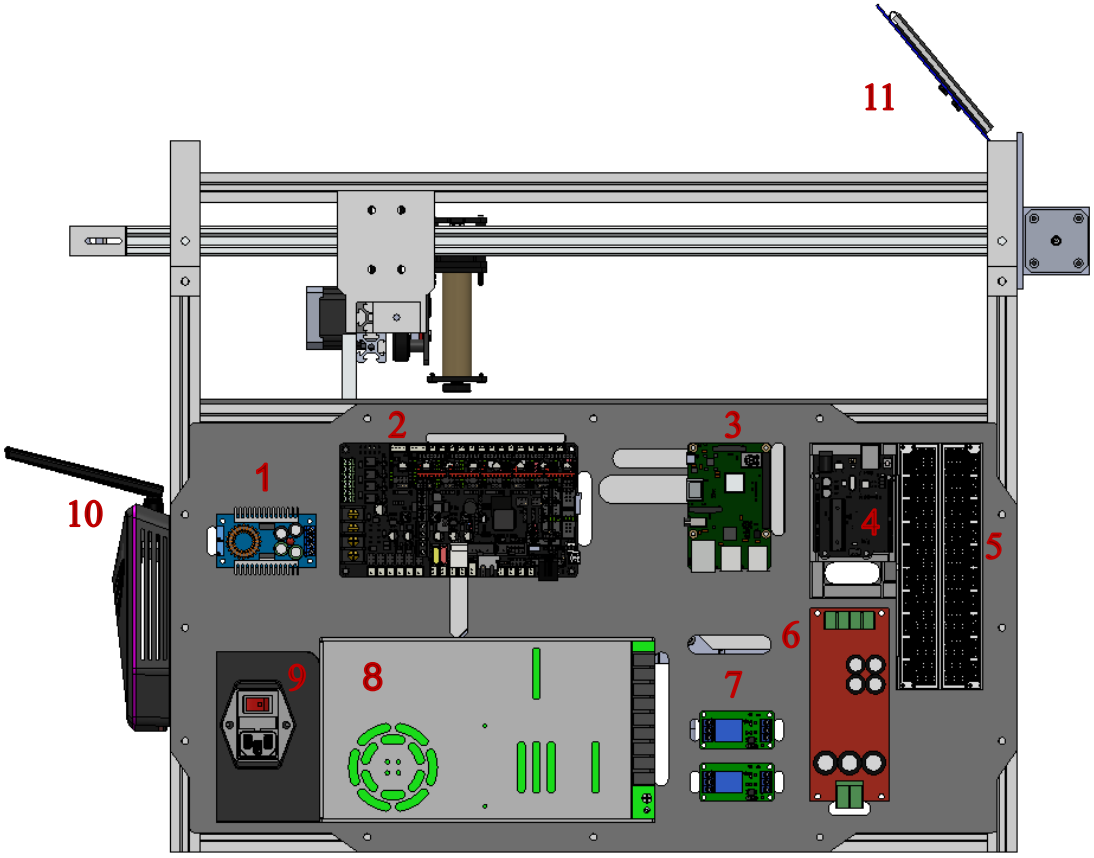

Figure 4: Left-Hand Side View of Printer Assembly Detailing Electronics Mounting Plate

Table 1: Electronics Hardware Specifications of the Machine

Component Number	Supplier	Model
1	DROK	DC 24V to 12V CC CV Step Down Voltage Regulator
2	Makerbase	MKS Monster 8
3	Raspberry Pi	Pi Model 4B
4	ELEGOO	UNO R3 Atmega328P
5	ELEGOO	Breadboard 830 Point
6	Diymore	1200W DC Module, 20A Adjustable Step-Up Power Supply Module 8-60V to 12-83V
7	AEDIKO	DC 12V Relay Module, 1 Channel Relay Board with Optocoupler Isolation Support, High or Low Level
8	DROK	0-24V, 480W, Variable Power Supply
9	POLISI3D	15A 250V Rocker Switch Power Socket, 10A Fuse
10	Netgear	N300 Wifi Router
11	Hosyond	7 inch IPS LCD Touch Screen Display Panel, 1024x600 Capacitive Screen

Initially, the BigTreeTech (BTT) SKR 1.4 Turbo was selected to host the Klipper firmware for its speed, reliability, number of serial communication interfaces, and its extensive user base. This motherboard operates at a 5V logic level which is required by the XAAR128. However, it was discovered that the maximum frequency of output logic signals of the BTT SKR 1.4 Turbo was 400KHz. This maximum logic frequency did not suffice for communication with the XAAR128 Print-head because it requires at least a 1MHz logic frequency.

The BTT motherboard was replaced with a Makerbase MKS Monster 8 because it was able to meet the frequency requirements of the XAAR128 and it touted a selectable logic level of either 3.3V or 5V. However, it was discovered that the Makerbase MKS Monster 8 does not have a selectable logic level and could only operate at a logic level of 3.3V. To mediate this issue, motherboards of the correct logic level and sufficient maximum logic frequency were sought but none were found.

An auxiliary logic level shifter. The BSS138 and TXS0108E logic level shifters were tested. A voltage plot of the communication signal transmitted by the BSS138, intended to have the form of a square wave, is shown in Figure 5 below.

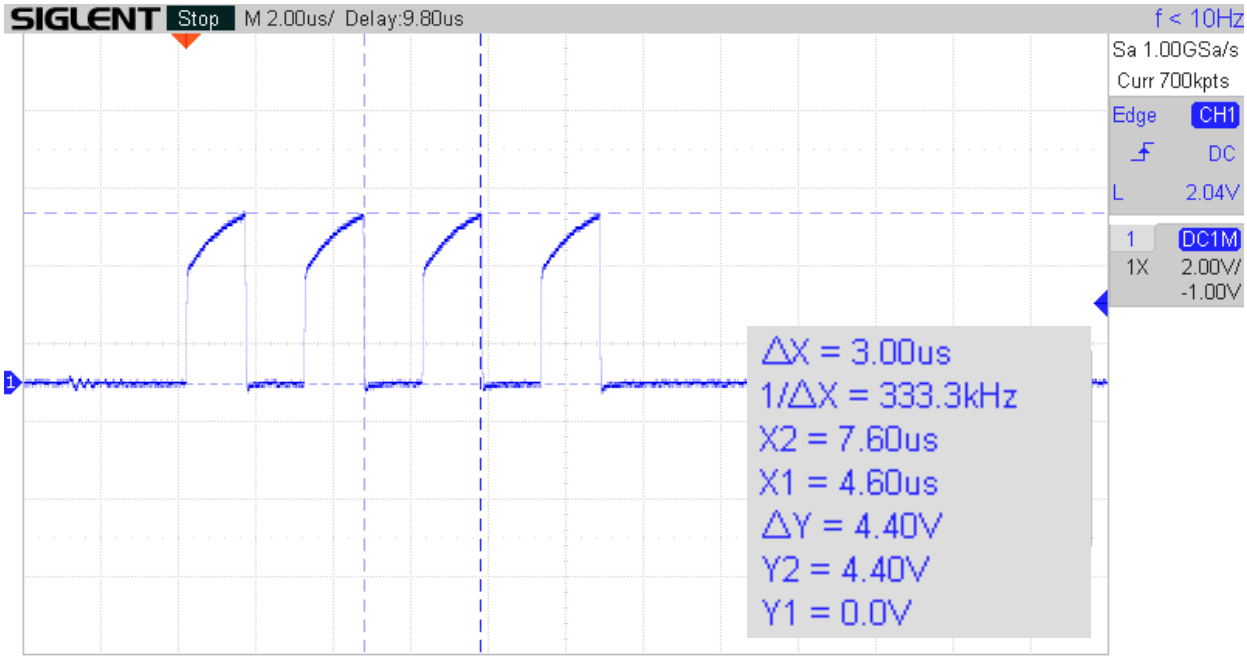

Figure 5: Pull Up Resistivity of BSS138

Figure 5 demonstrates the insertion loss found inherent to the BSS138 logic level shifter. Although the voltage level approached the required 5V, the insertion loss was far too great at the microsecond time scale to reach 5V and successfully communicate with the print-head. The BSS138 was replaced with the TXS0108E logic level shifter because it incorporated gain and active pullup features to mitigate problems with insertion loss. A voltage plot of a communication signal transmitted by the TXS0108E is shown in Figure 6 below.

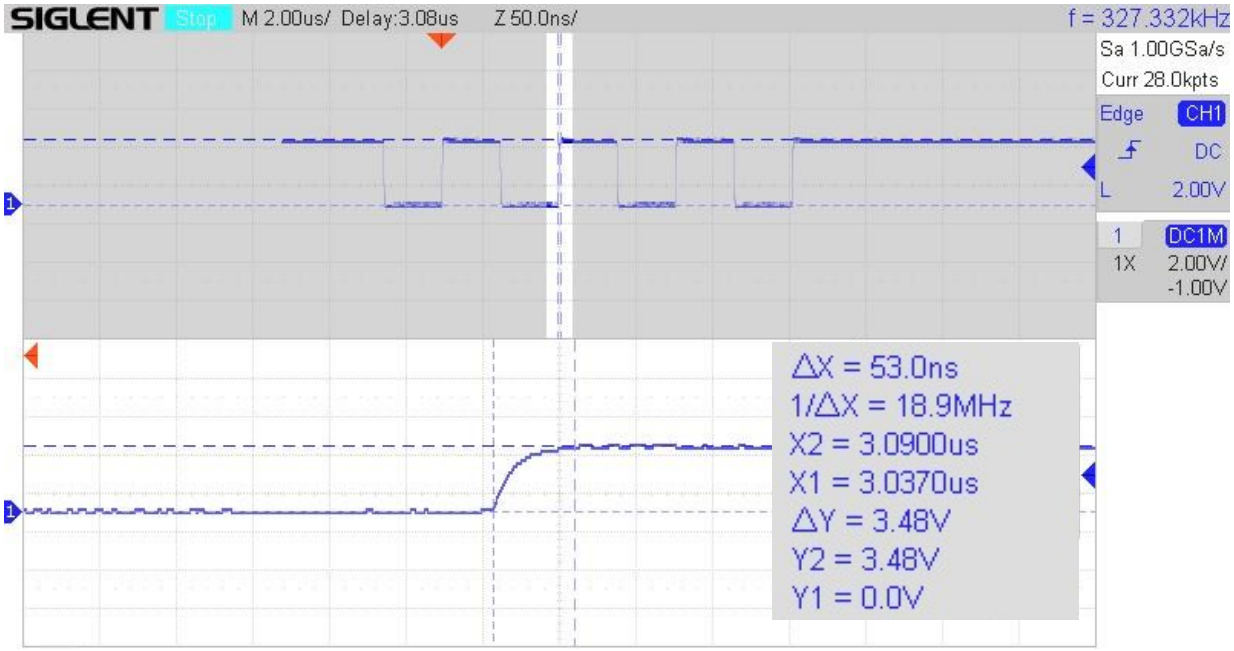

Figure 6: TXS0108E Rise Time Detail

Figure 6 shows that the TXS0108E fixed the issues with pull up resistance and insertion loss inherent to the BSS138 at the microsecond time-scale. The signal rise time of the TXS0108E was measured at 53.0 ns. This rise time was well within frequency requirements designated by the print-head. However, the risen voltage level did not meet the 5V requirement set by the print-head. However, the signal clarity was sufficient enough to develop and test the functionality of the SPI communication protocol required by the print-head. Development of the SPI protocol was conducted while in search of a sufficient logic level shifter. A successful test of SPI transmission is shown in Figure 7 below.

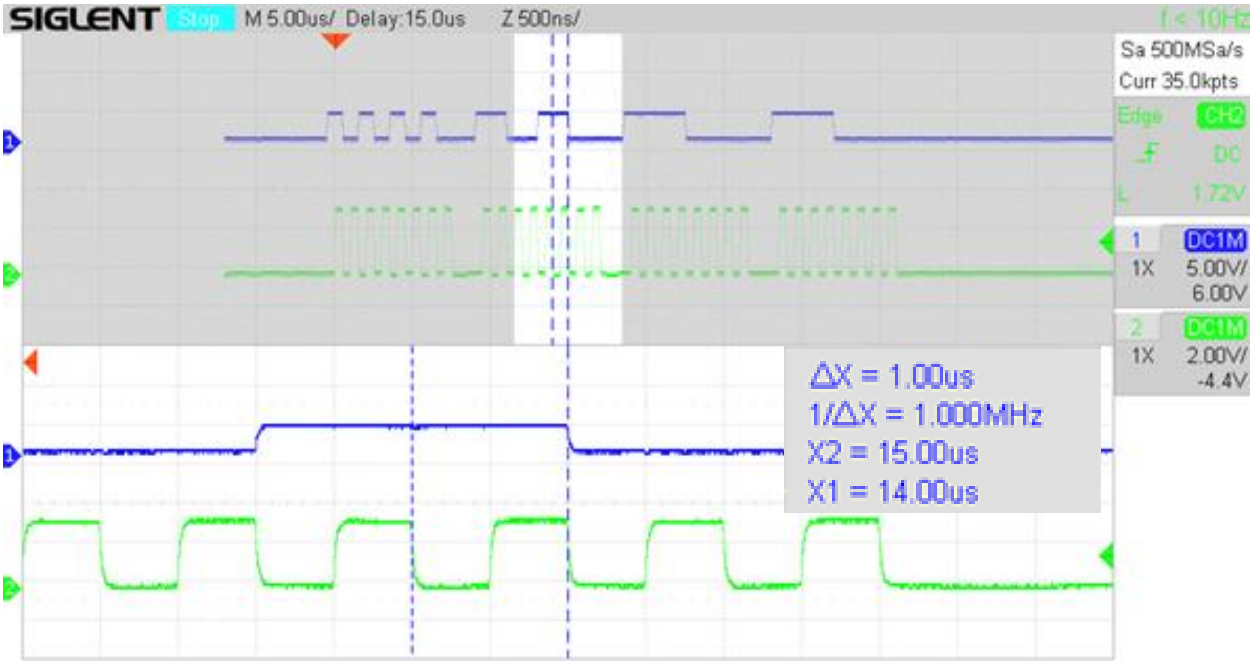

Figure 7: SPI Signals Test Detail

Figure 7 shows sufficient and parallel timing of the SPI MOSI and CLOCK signals transmitted by the TXS0108E logic level shifter. This voltage plot also demonstrated the success of SPI protocol implementation in the software print-head control module discussed later in Chapter 3.3.

A separate clock signal was necessary for timing of the XAAR128 state machine. The AD9833 chip was implemented to generate the 1Mhz clock signal. Figure 8 below shows the operation of the clock signal in reference to the accompanying communication signals transmitted to the XAAR128 print-head.

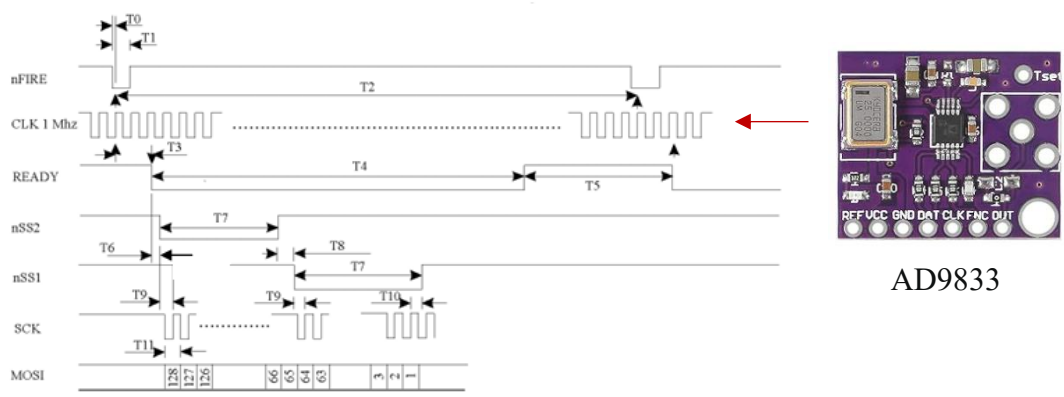

Figure 8: Implementation of AD9833 and Other Relevant Signals

It was verified that the AD9833 could generate the necessary clock signal. The development of necessary software to manage the other relevant signals is discussed in Chapter 3.3.

Because the TXS0108E could not sufficiently shift the 1MHz square wave signals, the decision was made to swap out the XAAR128 print-head for a diode laser and, thereby, convert the printer into an SLS/SLM machine. The conversion to a diode-laser print-head is discussed in Chapter 3.4.

3.3 Development of a Klipper Module for Control of a XAAR128 Print-head

The modular architecture of the Klipper software suite allowed for a higher degree of customizability and extensions of functionality over Marlin and other printer firmwares. The software, called Klippy, that runs on the Raspberry Pi initializes using a configuration written by the machine developer to configure Klipper for the specific the machine specific hardware. In this configuration file, the machine developer adds sections, corresponding to names of helper modules, that incorporate specific control and communication schema for the necessary components. For example, there is a different helper module for each type of motor driver.

The open-source nature, popularity, and extensive documentation of Klipper allow makers to create their own modules for novel hardware or sensor implementations. For this project, it was

necessary to develop and integrate a helper module for the XAAR128 print-head. This helper module was necessary because it allowed for precise timing of print-head control signals in parallel with gantry-motor drive control.

The requirements of this helper module are as follows:

- The module must be able to power cycle the print-head off and on
- The module must handle generation of transmission signals to the print-head for loading data into the XAAR128 registers and firing the nozzles.
- The module must handle signals received from the XAAR128 print-head for timing of the print-head state machine.
- The module must integrate GCODE macros for abstracting nozzle firing commands

The control schema of the print-head was retrieved from the XAAR128 Operation Manual. This manual includes instructions for print-head mounting, communication, fluid supplication, and maintenance. The helper module was developed referencing this operation manual.

The helper module written for XAAR128 control can be found at https://github.com/skbrownlee/klipperXAAR128dev/blob/XAAR128/klippy/extras/xaar128.py

The initialization of the module in the printer.cfg file registers the following GCODE commands:

- “HEAD_ON”: Power cycles the XAAR128 into the ON and READY state with proper sequencing so no damage is incurred.
- “HEAD_OFF”: Power cycles the print-head off with proper sequencing so no damage is incurred.
- “L1 HXXXXXXXXXXXXXXXX”: Loads and fires the print-head’s 128 nozzles and ensures the XAAR128 reenters the READY state. This command takes 16 Hexadecimal

digits after the ‘H’ parameter and sends them in a sequence of 8-bit SPI messages to the print-head MCU to be registered in the buffer and subsequently fired. This process takes ~0.14 ms. Note that the ‘X’ characters in the command are placeholders for each of the 16 hexadecimal digits.

A pull request to the Klipper main repository on Github, for adoption of the module, was not submitted because the available logic level shifters were not capable of complete hardware testing of the module. The communication protocol and power sequencing protocol were tested and verified using a Siglent Technologies SDS1104X-E 100Mhz Digital Oscilloscope with 4 Channels. An example of an L1 command input in the machine console is shown in Figure 9 below. Note that the resulting signals in Figure 7 correspond to the highlighted command shown in Figure 9.

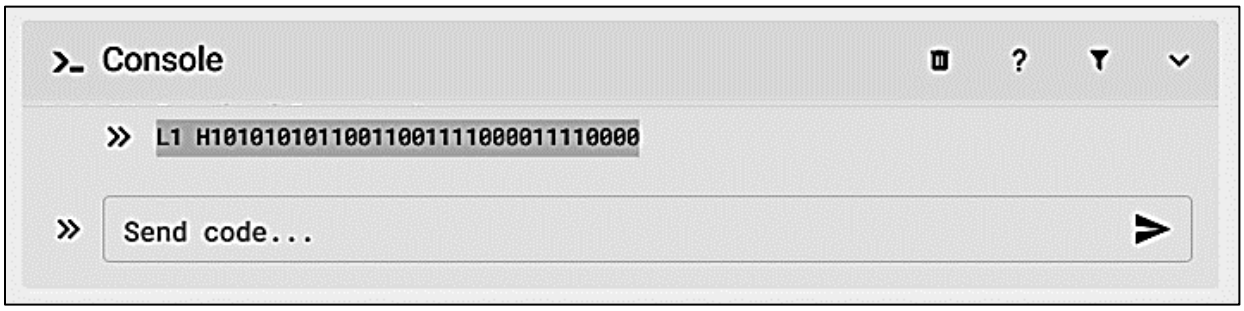

Figure 9: Example of L1 HX Command Input to Printer Machine

At this stage, the serial communication was properly timed and sequenced by the module. However, the logic voltage level did not meet the 5V requirement specified by the XAAR128 print-head. A suitable logic level shifter was not found.

The development of the control system for the XAAR128 print-head was halted by failure to implement logic level shifting. This was the only functionality necessary to demonstrate BJAM using the machine. At this point, the decision was made to modify the machine to investigate SLP.

3.4 Conversion to Diode Laser Print-head

Although the control issues regarding the XAAR128 print-head bottlenecked progress, the state of the machine provided a good basis for powder bed additive manufacturing. The available options for converting the machine to perform alternative processes were EBM, SLS, or SLM. Without the build volume of the machine enclosed in a vacuum chamber, EBM was not possible with the machine. A low-cost laser was selected to replace the binder jetting print-head. The laser selected was the LASER TREE LT-40W-AA 12V. The laser consumes 40W and produces a 450 nm wavelength beam with an optical power of 5W. The laser was installed on the machine and experimentation of SLS and SLM began.

Without a vacuum chamber or inert gas chamber, material selection was limited to non-reactive materials. These materials include polymers, ceramics, and composites. Metals were not considered due to the probability of metal dust deflagration. It was discovered in preliminary testing of materials that the available laser could sinter and melt SiC substrates as well as SiO_2 powder. However, all samples fabricated using SEDs too low to form a melt pool were too fragile to transport. Therefore, the controlled experimentation of SLM of SiC and SiO_2, as well as their composites, formally began.

The laser was mounted to the print-head carriage and laser power was supplied by one of the 12V fan output pins available on the printer motherboard. The M3 and M5 GCODE commands were implemented and instructed to turn the laser on and off respectively. The default power setting when the M3 command is ordered is full power which is 5W.

The M3 command can be followed by an ‘S’ parameter and a number ranging from 0 to 255 to specify the ‘power’ setting of the laser from 0-100% respectively. However, the on state of this

laser is continuously triggered by the high state of a PWM signal. Because of this, the parameter is only capable of modifying the pulse duration of the beam and any value other than full power results in a discontinuous beam. In powder bed fusion selective laser processing, pulsing the laser at constant velocity results in regular spaces of entirely unaffected powder. It is possible to mitigate this problem using complex path strategies. However, to maintain simplicity, the laser power was not varied in any of the experiments.

3.5 Rotary-Cylinder-Recoater Mechanism Design

It was discovered that the machine's recoater blade was of insufficient rigidity to apply a smooth and flat layer of powder. Many research and industrial printers utilize a counter-rotating rolling cylinder mechanism for recoating the print bed with a layer of powder substrate. This mechanism is commonly used because it is capable of assisting with powder compaction during the recoating process [33].

A rotary-cylinder-recoater mechanism was designed and constructed for the machine. The design of the mechanism can be found in Figure 11 below.

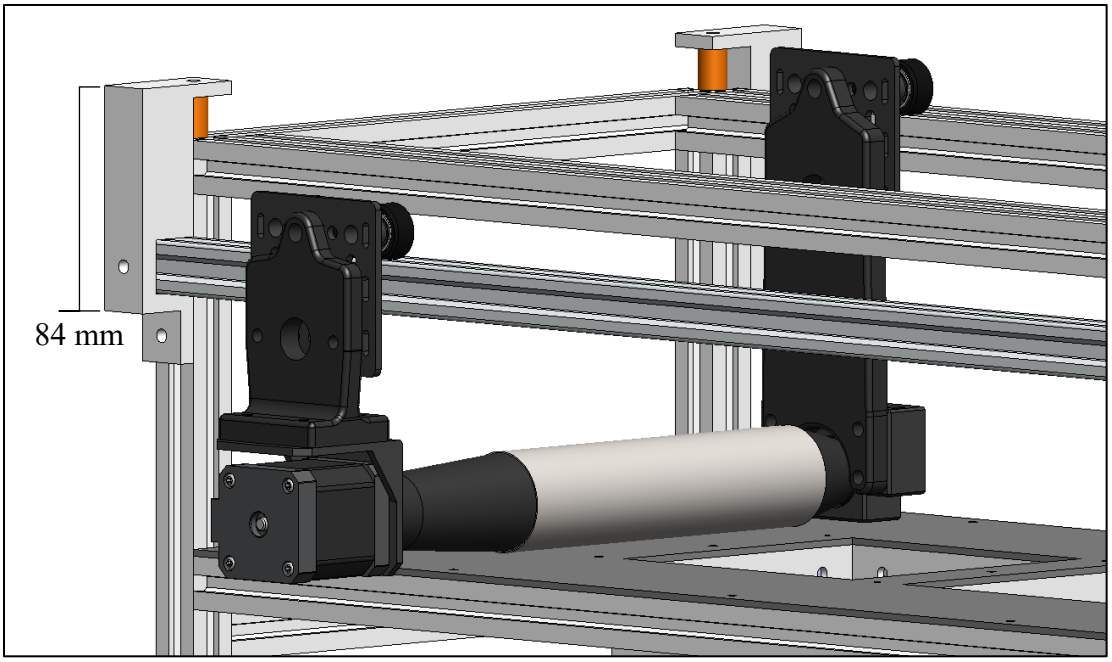

Figure 10: Render of Roller Pusher Mechanism

The rotary-cylinder-recoater mechanism was installed as shown in Figure 11. However, the parallelism of the gantry, compliance in the mechanism, and the single-side drive configuration each contributed to binding of the mechanism. The rotary-cylinder-recoater mechanism would need to be redesigned with dual-drive of the carriages and increased rigidity to perform rotary-cylinder recoating and compaction of the substrate. This mechanism was stripped in favor of a solid recoater blade.

3.6 Recoater-Blade Mechanism Redesign

A recoater blade mechanism was designed and affixed to the print-head rail. Attachment to the same rail structure that the print-head was mounted to ensured that the powder layer remained at a fixed distance from the laser print-head. Furthermore, this ensured that the focal point of the laser remained at the same location relative to the surface of the substrate. The substrate interfacing face of the recoater-blade was polished to a mirror finish to ensure interference and

erroneous dragging of particulate by the recoater-blade was minimized. The recoater-blade is shown in blue in Figure 12 below.

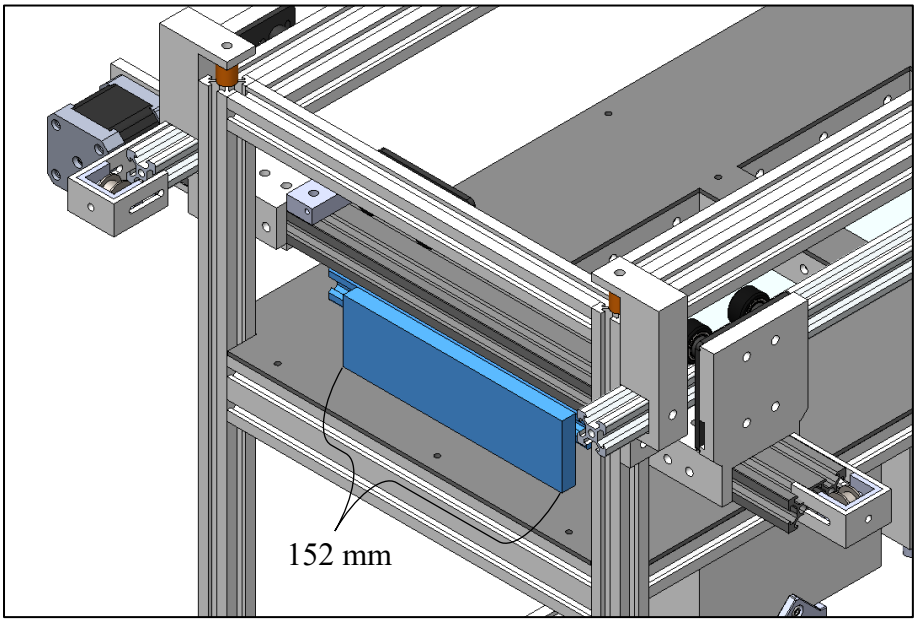

Figure 11: Render of Rear Left Isometric View of Recoater Blade

The recoater blade showed significant improvement over the previous design and it produced substrate powder layers flat enough to form continuous line specimens. This recoater-blade was used in all controlled fabrication experimentation.

3.7 Machine Specifications

The SLP machine developed consists of an aluminum extrusion frame and various components that form a print bed, a supply bed, and a cartesian gantry system. Diagrams of the top and bottom view of the machine highlighting the coordinate system and major components are shown in Figure 13 below.

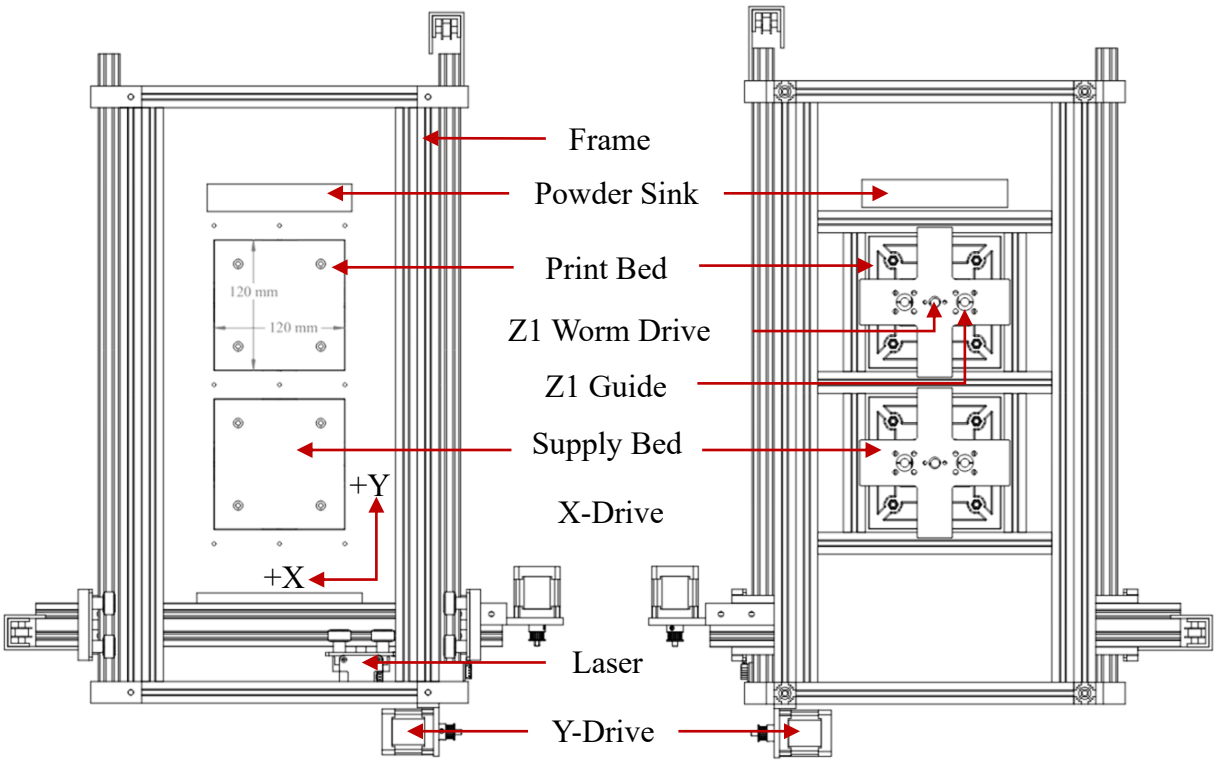

Figure 12: Top View (Left) and Bottom View (Right) of the Machine at Home with Axes and Notable Components Labeled

The machine home was the origin of the coordinate system shown in Figure 13. Also, note that the origin was on the far side of the supply bed relative to the print bed. This configuration placed the print bed origin at machine coordinates $(+5\,\text{mm}, +220\,\text{mm})$. The print bed dimensions placed maximum print X at machine $X = 130\,\text{mm}$ and maximum print Y at machine $Y = 330\,mm$. The recoater-blade cleared the powder sink at $Y = 365\,\text{mm}$. Therefore, to properly dispose of excess powder, the recoater-blade traversed to $Y = 365\,\text{mm}$. The free-fitting tolerances at the outer perimeter of the print-bed and supply-bed, between the walls the bed surface, allowed powder to spill off the powder-beds. This spillage formed a ravine at the perimeter of the powder-bed surface. This phenomenon decreased the usable size of the print-bed to the central $115 \times 115\,\text{mm}$ square of the print-bed, which remained unaffected by spillage.

The substrate must reach the recoater-blade for surfacing and leveling of the substrate. The print-bed, when homed, required 30mL of powder substrate to reach the height of the recoater-blade.

3.8 Recoating Procedure and GCODE Macro Implementation

A recoating procedure was developed to handle powder spreading/ powder layer application on the print bed. The steps of the recoating procedure were defined as follows:

1. The print-bed moves in Z+ direction by the layer height, h.
2. The Y-Axis moves to the machine home along with the affixed recoater-blade.
3. The supply bed moves in the Z- direction by $c \cdot h$, where c is the supply factor.
4. The Y-Axis moves across the beds to the end of the track.
5. The Y-Axis returns to machine home.

It was discovered that the X position of the print-head deforms the X-Axis track of the gantry enough to drag powder during the print; therefore, another step was added between Step 3 and 4 to move the print-head to the center of the beam (X=+130 mm). In this way, the recoater-blade remained at its minimum height during the recoating process.

GCODE Macros were added to the printer configuration file to control the recoater-blade.

- RECOATER_PULL: Moves Y axis to Home
- RECOATER_PUSH: Moves Y axis to +330 mm
- RECOAT: Adds layer to build plate according to recoating procedure

3.9 Development of an FDM to SLS/M GCODE Converter

Open-source slicers for 3D printers available at the time were designed and configured for use with FDM 3D printers. It was necessary to develop a script that could convert GCODE file output

from FDM based slicers to work with the GCODE commands necessary for laser control. A GCODE converter was developed to modify the files output by an FDM slicer into a form readable by the printer. This converter removed stepper advance codes, denoted by 'AXXX', in the FDM GCODE script. These codes were used to control filament extrusion and were not necessary in the SLM process. The converter script adds the GCODE macros for controlling laser power and new layer application to the original GCODE script. This script was open sourced and can be found at https://github.com/skbrownlee/FDM-GCODE-to-SLS-GCODE-Converter.git.

This converter was used to generate GCODE scripts for fabrication of preliminary specimens of complex geometry with implementation of complex scanning strategies. However, the specimens fabricated in this stage exhibited substantial defect formation and were too fragile for transport.

3.10 Preliminary Fabrication Experimentation

Preliminary testing of the machine began with various substrate mixture contents of SiC and process parameters. This experimentation proved the capability of the machine to form a melt pool of the chosen substrates. It also proved that fabrication of line and square specimens, strong enough to survive transport, was viable.

One of the first fabricated line samples was optically imaged and is shown in Figure 13 below.

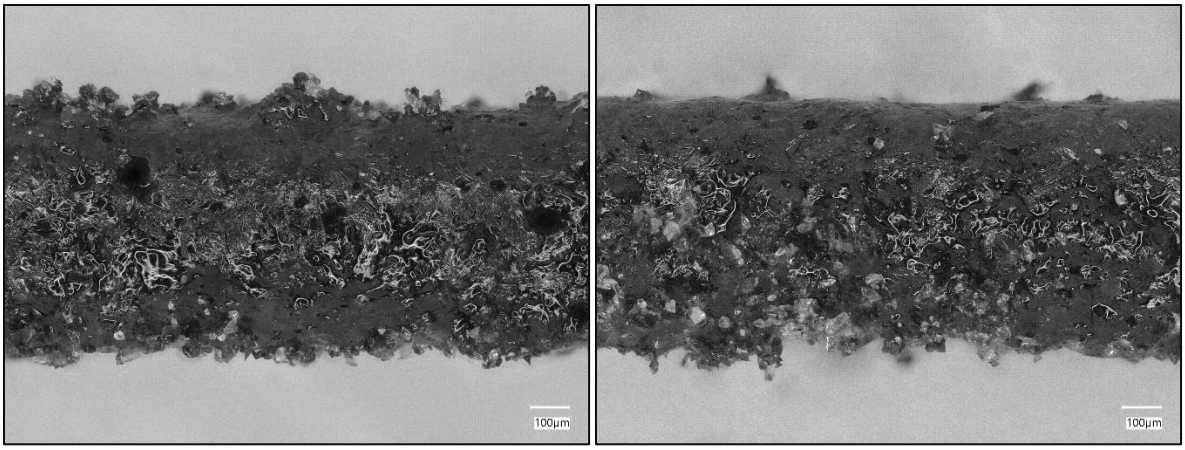

Figure 13: Top-View (Left) and Side-View (Right) Images of a Line Specimen Fabricated using 100% SiC Substrate

Initial inspection of preliminary samples revealed that direct SLM of SiC substrates is possible, but fabrication of parts using this method demands careful control of the process parameters. Optical images were taken at higher magnifications to qualitatively investigate the nature of the solidified melt pool. These images are shown in Figure 15 below.

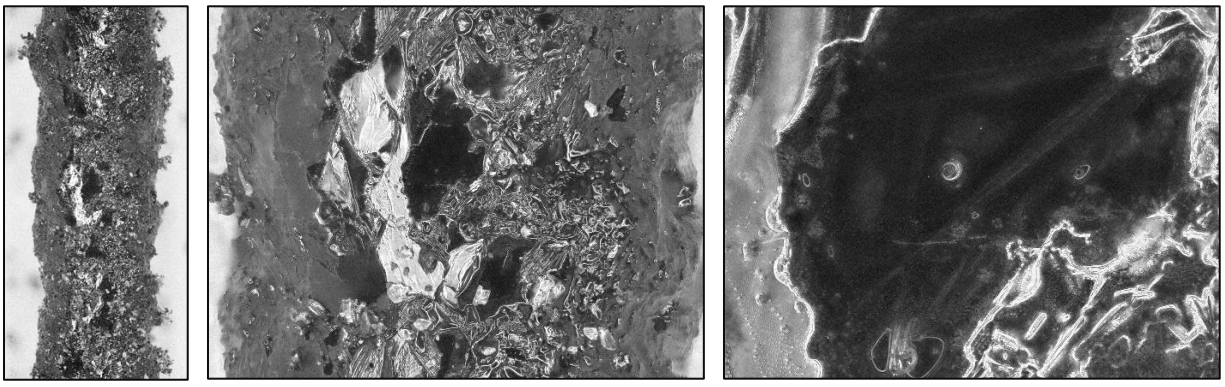

Figure 14: 100% SiC (Left to Right) 80x, 300x, 1500x

It can be observed in Figure 15 that large grain crystal structures were formed by solidification of the melt pool. The top of the fabricated line often incorporated large clear crystals of lower porosity than the surrounding material. These crystals may be SiO_2, or a form of quartz. The dark regions may be composed of SiC or a blend of Si, C, and SiO2. Compositional analysis and a study of the crystallography are necessary to attain certainty of the composition of the fabricated parts.

3.11 Experimental Design 1: Line Specimen Fabrication

Before lines can be added together to create two-dimensional layers, an investigation of line fabrication must be conducted to characterize the line fabrication process. An experiment was designed to discover and document the effect of process parameters on lines fabricated SLM of SiC/SiO_2 substrates.

The first parameter of interest in the characterization of line fabrication is the material makeup of the powder substrate. The powdered SiO_2 and SiC used were selected for their granularity based on literature investigating the effect of particle size and shape on the powder bed fusion process [34]. The specifications of the powders selected are listed in Table 2 below.

Table 2: Powder Supply Information

Manufacturer	Chemical Makeup (Purity)	Model	Average Particle Diameter
SACKORANGE	SiC (N/A)	Step-3 500 Grit Silicon Carbide Rock Tumbler Grit	50 μm
LFA Machines	SiO_2 (N/A)	Silicon Dioxide Anticaking Agent	20 nm
Chemsavers	SiO_2 (99.5%)	Silicon Dioxide (Silica), Powder – 325 Mesh	57.8 μm

Eight substrate mixtures were tested in total. Seven, two-part, powder mixture substrates of SiC and SiO_2 were prepared for line fabrication experimentation. All substrate mixtures were prepared using noncompacted volumetric parts of the constituents. SiC was used as the base constituent; therefore, the noncompacted volume fraction of SiC in the substrate mixture was often used to refer to the material content of the substrate mixture for succinctness. The mixture content of SiC was varied in increments of 10 vol%. from 70-100 vol% in mixtures containing SiO_2 powder additive of 20 nm average particle diameter (20 nm SiO_2). The mixture content of SiC was varied

in increments of 10 vol% from 60-100 vol% in mixtures containing SiO_2 powder additive of 57.8 μm average particle diameter (57.8 μm SiO_2). A substrate containing only the SiC powder was also subject to the fabrication experiment (100% SiC).

Substrate mixtures containing concentrations of SiC less than 70 vol% with 20 nm SiO_2 (70% SiC, 20 nm SiO_2) and mixtures containing less of SiC less than 60 vol% with 57.8μm SiO_2 (60% SiC, 57.8 μm SiO_2) were found unsuitable for the printing process. This instability was due to the ready agglomeration of the SiO_2 particulate on the millimeter scale. This aggregation was likely caused by humidity in the environment [35]. Millimeter scale agglomerations were not tolerated because homogenous agglomerations at the scale of the laser focal point would lead to suboptimal mixing and destabilization of the melt pool.

Magnified images of the powder mixture were taken with a Keyence VHX-7000 Optical Microscope to verify consistency and ensure millimeter-scale agglomerations did not readily form in the powder. The substrate mixtures containing the highest and lowest concentrations of SiC tested are shown in the figures below. The text box in the figures denotes the length of the white scale bar.

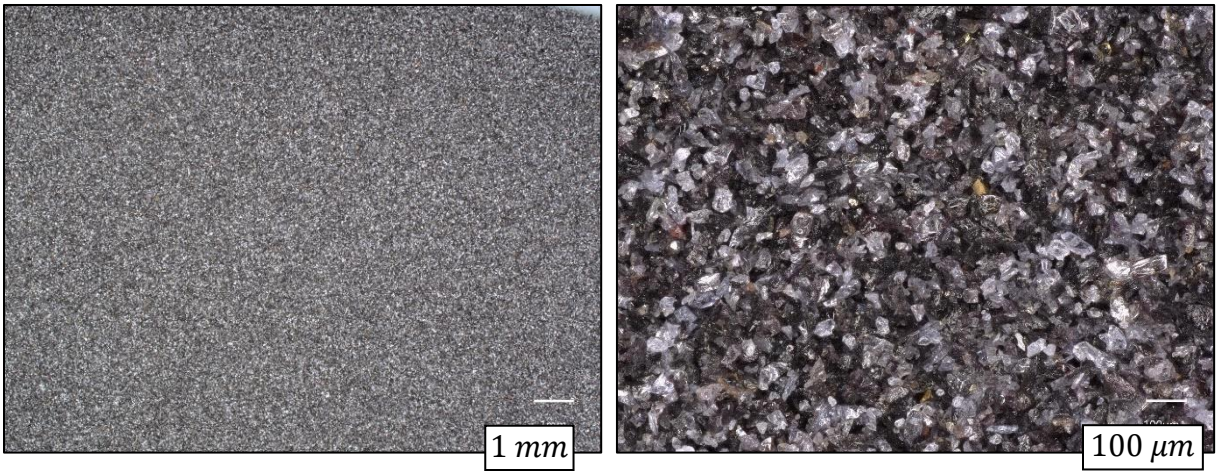

Figure 15: 20x (Left) and 200x (Right) Optical Images of 100% SiC Substrate

Figure 16 shows the 100% SiC substrate. The average grain size specified by the supplier is present and impurities are heterogeneously mixed enough to not appear at the millimeter scale.

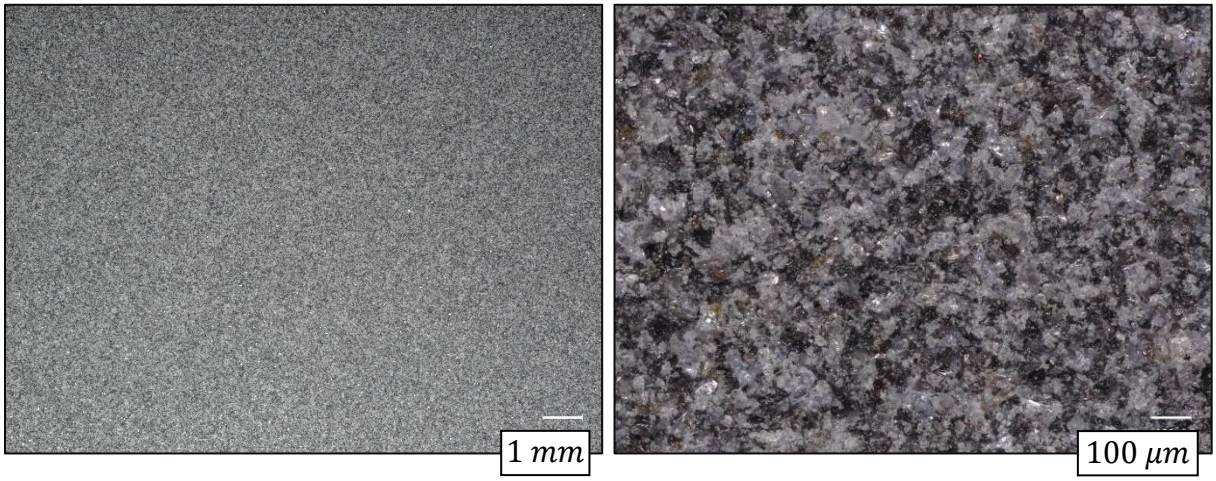

Figure 16: 20x (Left) and 200x (Right) Optical Images of 60% SiC, 57.8μm SiO_2 Substrate

Figure 17 shows that microscale agglomeration and clustering of SiO_2 formed in the 60% SiC, 57.8 μm SiO_2 substrate; however, millimeter scale agglomerations remained absent.

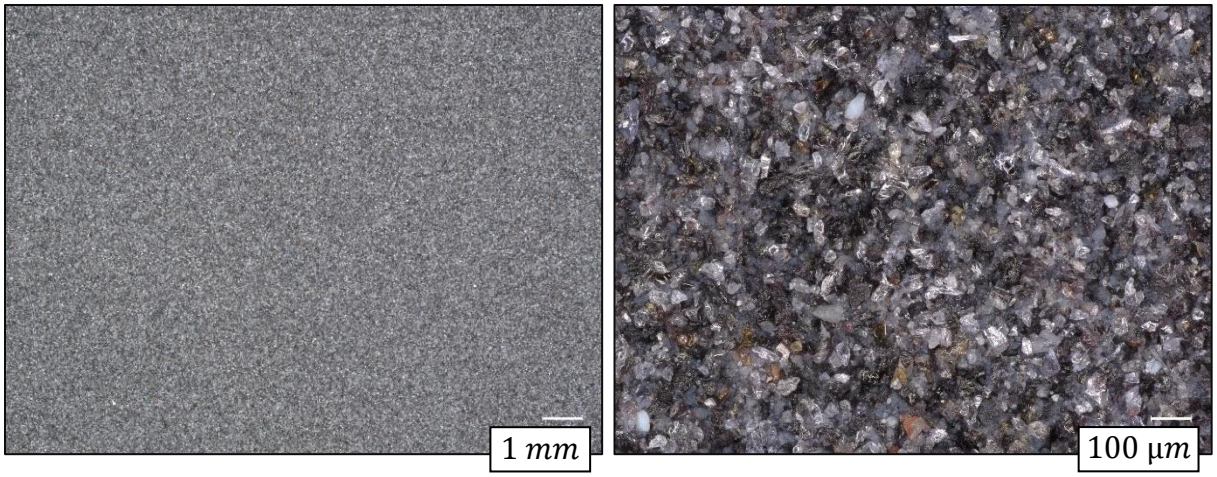

Figure 17: 20x (Left) and 200x (Right) Optical Images of 70% SiC, 20nm SiO_2 Substrate

Figure 18 shows the microscale agglomeration of SiO_2. Cloudy agglomerations of nanoscale SiO_2 crystals can be seen approaching 30 µm in diameter.

These eight substrate mixtures were each tested in the fabrication experiment alongside the second process parameter of interest.

The second process parameter of interest in the line specimen test is the SED (SED). Because the laser power and spot diameter are fixed by the machine configuration, the scanning velocity is the only parameter left capable of directly influencing the SED as shown in Eq. 1. Therefore, the scan velocity was directly varied in the experiment to indirectly vary the SED.

In development of test print procedures for single layer prints, it is prudent to print multiple samples in one run. Within this single layer, the print parameters of interest can be varied for experiment. However, currently available slicers do not permit variations of print parameters within a single layer. Therefore, a GCODE script was manually written for this experiment.

The print-bed was long enough to host nine rows of 20 mm line specimens; these rows were numbered 1 to 9 on the print bed. The line specimens of each row were designated by their ordered number. There was enough additional space on the print bed to replicate the line specimens in two additional columns for triplication for a total of twenty-seven line specimens per print. The three

columns of triplicate specimens on the print bed are designated A, B, and C. A diagram of the specimen layout on the print bed is shown in Figure 19 below.

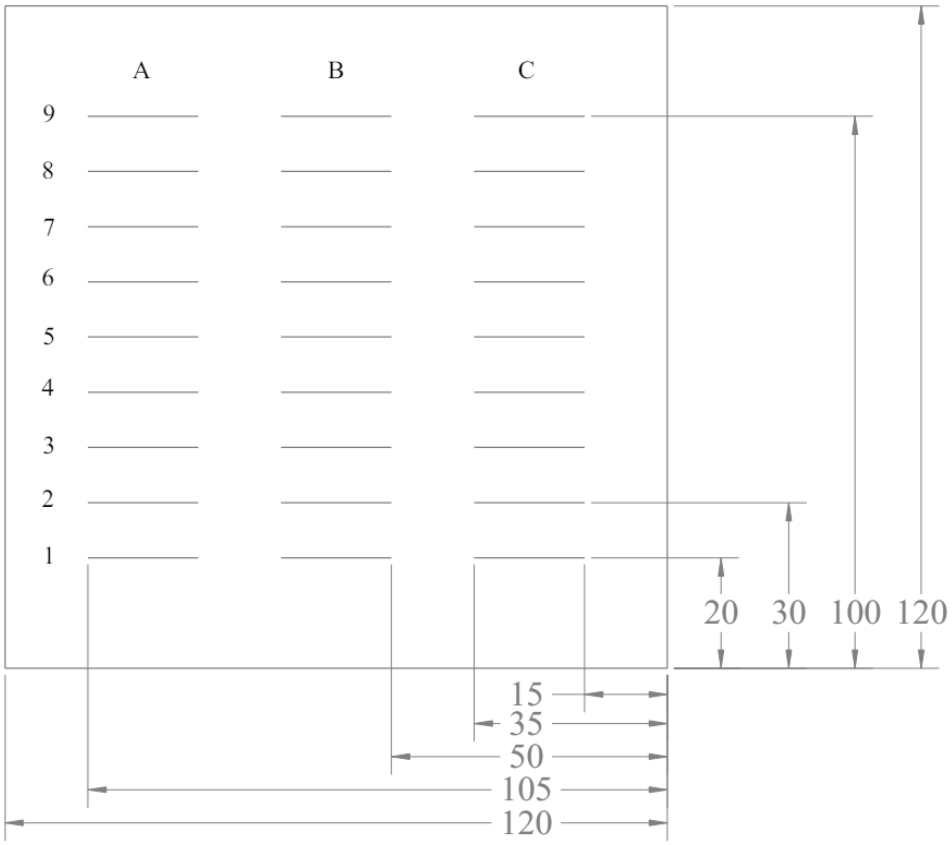

Figure 18: Diagram of Line Specimen Test Print Bed Layout (all dims. in mm)

The geometry shown in the diagram of Figure 19 was referenced in development of the GCODE script and was maintained throughout experimentation. In this study, individual samples are referred to using a column-row notation. For example, the sample located in column A and row 1 is denoted as “Sample A1”. This notation is used throughout the paper to identify specific samples within the dataset.

Negative Y moves of the gantry were found to occasionally disturb the powder bed surface. Therefore, the script directs the machine to scan the columns sequentially in order by row from 1 to 9. This was done to ensure that the recoater-blade, attached to the gantry, never moved in the

negative Y direction during the print. This ensured that the powder surface was undisturbed by the recoater-blade while scanning.

The SEDs chosen for experimentation range from 0.05-0.45 J/mm^2 increments of 0.05 J/mm^2. SEDs less than 0.05 J/mm^2 often resulted in bubbling and stagnation of the melt pool. Samples fabricated using SEDs greater than 0.45 J/mm^2 were often broken in transport during preliminary testing.

The manually generated GCODE script uses a different SED for each row of three line specimens. The SED used by the GCODE was formulaically determined by the minimum and maximum SEDs subject to experimentation. The formula for SED based on the row of the line specimen is given as:

$$q = \frac{O_n}{20} \qquad \text{Eq. 3}$$

where q is the SED in J/ mm^2 and O_n is the ordered number of the row.

A 3D printable sample tray was designed for hosting and transporting line specimens from the print bed to the microscope. The tray is shown in Figure 20 below.

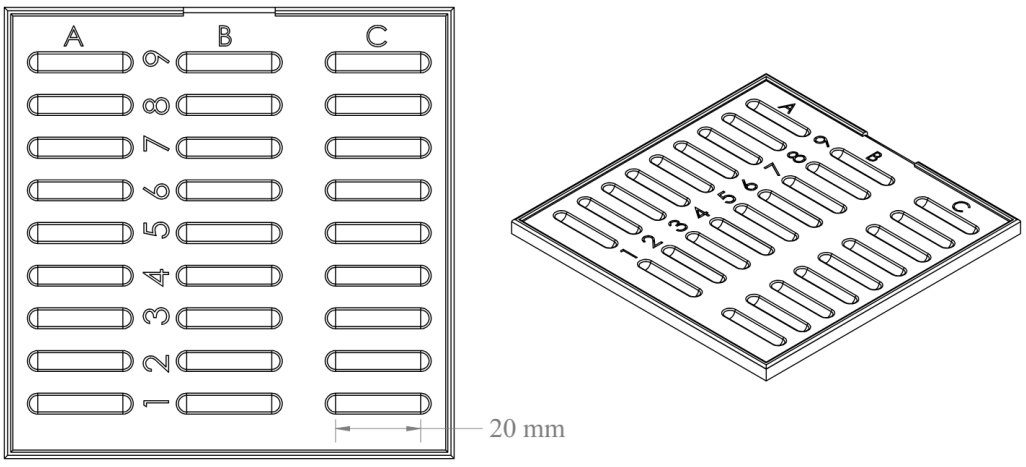

Figure 19: Line Specimen Tray

The specimen tray interfaces with 4 in. square acrylic sheets that form a transparent lid using tape as a hinge and clamp to seal the acrylic against the face of the pocketed surface. The acrylic sheet was removed for optical microscopy.

After a line specimen print was completed, the specimens were carefully removed from the build volume using fine tweezers and placed in their respective locations in the sample trays. The specimens were then mounted place individually by first brushing a photopolymer resin on one end of the corresponding pocket. Next, the specimen was placed in the pocket in the desired orientation. Then, the sealing surface was wiped with tissue paper. Finally, the resin was photocured with ultraviolet light. At this stage, the samples were transported to optical microscopy for data collection.

The line width data was collected using a Keyence VHX-7000 Digital Microscope. The center of each sample was imaged using depth composition at 50X magnification. The depth composition image was processed by the Keyence Software's Automatic Edge detection feature that marks high color contrasts between adjacent pixels within a manually selected pixel band. The machine then performs a linear least squares regression of the determined edge point locations to determine the line that represents the edges. The microscope defines the first selected edge as the datum to compute the parallel line that minimizes the R^2 value of the second edge data set. The distance between this parallel line and the datum is also the mean distance of the second set of points to the datum. This technique is useful for measuring edges of components fabricated by solidification of potentially unstable melt pools of potentially high irregularity. The distance between the lines is the width of the line sample. This procedure was performed for each line specimen. An example of a result of this procedure is shown in Figure 21 below.

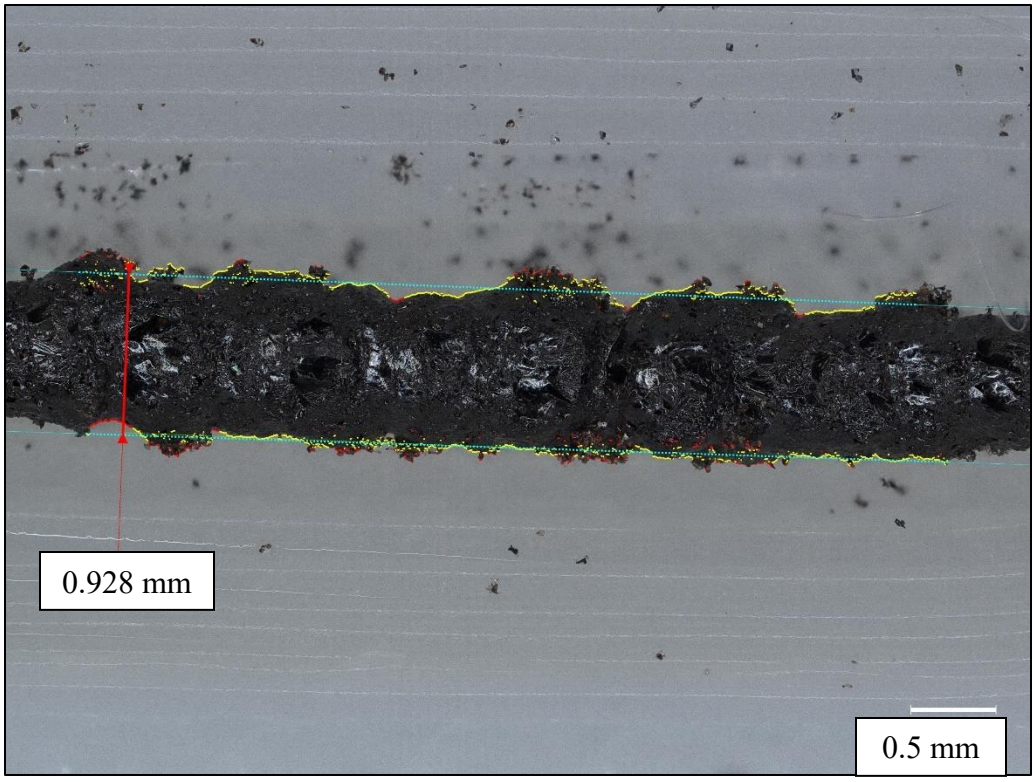

Figure 20: Example of Line Width Measurement Results of Keyence VHX-7000 on 100% SiC Sample A1

In Figure 21, the red dimension indicates the line width, the yellow dots indicate the edge points detected on the inner half of the selecting band, the red dots indicate the edge points detected on the outer half of the selecting band, and the cyan lines indicate the linear least squares regression line for the detected edge points. The faint green line extending from the middle of the lower edge of the specimen to the annotated dimension is the mean distance from the datum, the first selected edge, to the second set of points.

This distance data can be used to investigate the relationship between the SED and the resulting fabricated line width of the sample.

The Keyence parallel distance measurement software only outputs the computed distance and the image overlaid with the data discussed below Figure 21. Therefore, a MATLAB script was written to post process the images by extracting and analyzing the coordinates of the detected edge points.

The MATLAB script takes images as seen in Figure 21 as input. The method for analysis proceeded as follows:

1. The image was loaded into memory as a three-dimensional array of RGB color values
2. The user selected the midpoint of the line sample above the bottom edge and below the top edge using a spanning crosshair cursor (only performed on the first run).
3. Yellow dots for the top and bottom edge were detected and recorded separately.
4. A linear regression was performed for the two data sets.
5. The edge with the lower variance was selected as the datum.
6. The data was rotated about the image origin to detrend the images taken at an angle.
7. An offset was applied such that the middle of the line sample was zeroed to $Y = 0$.
8. The line width was computed, and the data table was updated.
9. Steps 1-8 were repeated for each sample.
10. The data was processed, and the figures were generated.

The dot detection method was verified by apparent non-occlusion of yellow pixels when the detected points were overlaid on the reference image. An example of the data after detection of the yellow pixels, as shown in Figure 21, is shown in Figure 22 below. Note that the stage shown was before the linear regressions were calculated and the data was rotated about the image origin.

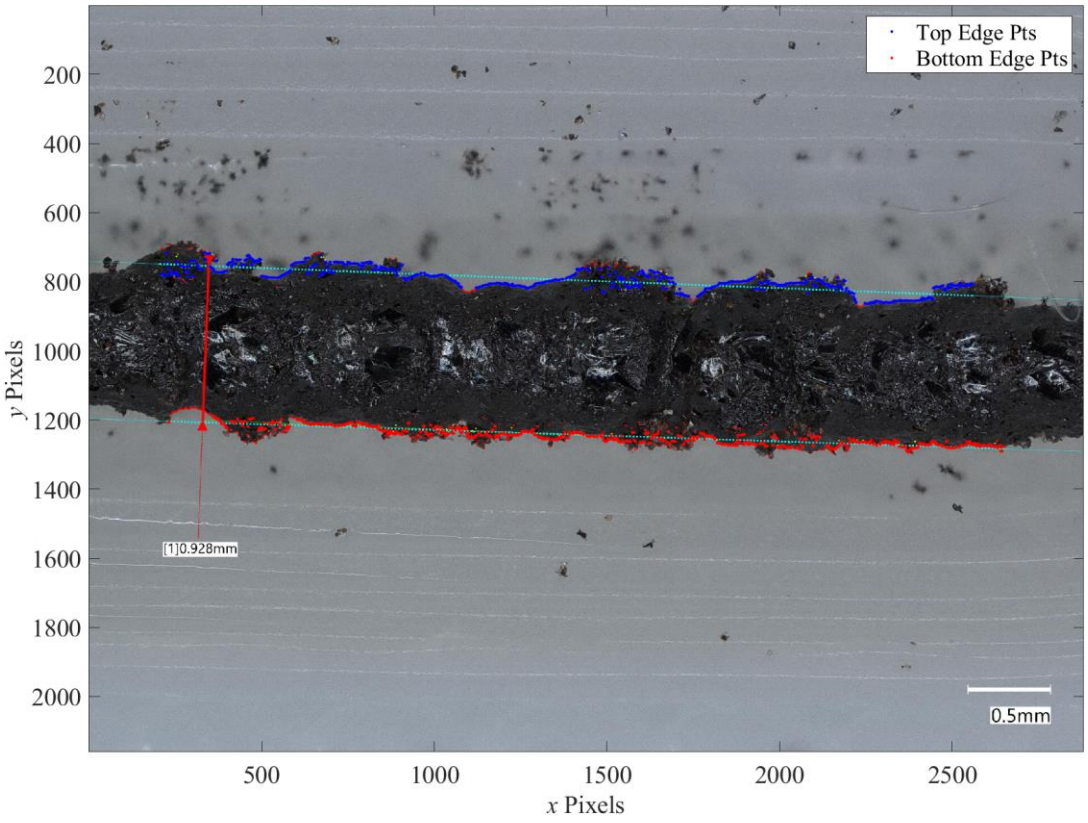

Figure 21: Example of Yellow Dot Detection Results on 100% SiC Sample A1

To compute the line widths of the samples given, the detected points were passed through a QR decomposition algorithm, built into MATLAB as the "fitlm" function, to create linear regressions of the detected points. The regression line having the lower of the two sums of the square resultants was chosen as the reference datum because the minimizer of the sum of the square resultants is a straight line. The arctangent of the slope of the datum relative to the image coordinate system provided the rotated angle of the sample in the image. The detected coordinates were then rotated about the image origin to detrend the regressions. An offset was then applied to the Y-Coordinates of the points to align the centerline of the sample with Y=0.

An example of the results of the image processing procedure is shown in Figure 23 below.

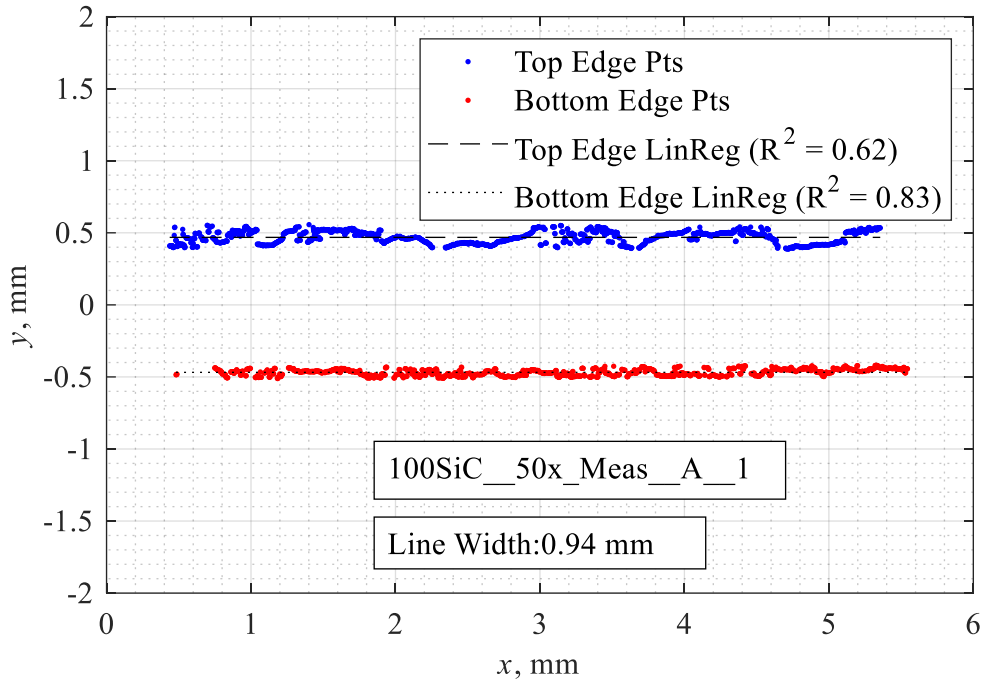

Figure 22: Example Processed Image Line Width Calculation for 100% SiC Sample A1

Figure 23 shows that the image processing and analysis method was capable of accurately capturing the edge contours of the fabricated line. It is worth noting that the aspect ratio of the original image was maintained in the figure(s) to standardize the initial visualization of the generated graphs.

At this stage, a Bland-Altman analysis was conducted to assess the agreement between the two different line width measurement techniques. Developed by J. Martin Bland and Douglas G. Altman, this method involves plotting the differences between the results of the two measurement techniques against their averages, allowing for inspection of any systematic bias and the range of agreement [36]. The mean difference, $\bar{d}$, provides an estimate of the systematic error. The limits of agreement indicate the range within which most differences between the methods are expected to fall. The limits of agreement are calculated as follows:

$$L_L = \bar{d} - 1.96 \cdot \sigma_d \qquad \text{Eq. 4}$$
$$L_U = \bar{d} + 1.96 \cdot \sigma_d$$

Where L_L and L_U are the lower and upper limits of agreement, respectively, and σ_d is the standard deviation of the differences in the data of the two methods.

The lower and indicate the range within which most differences between the methods are expected to lie. The result of the analysis is shown in Figure 24 below.

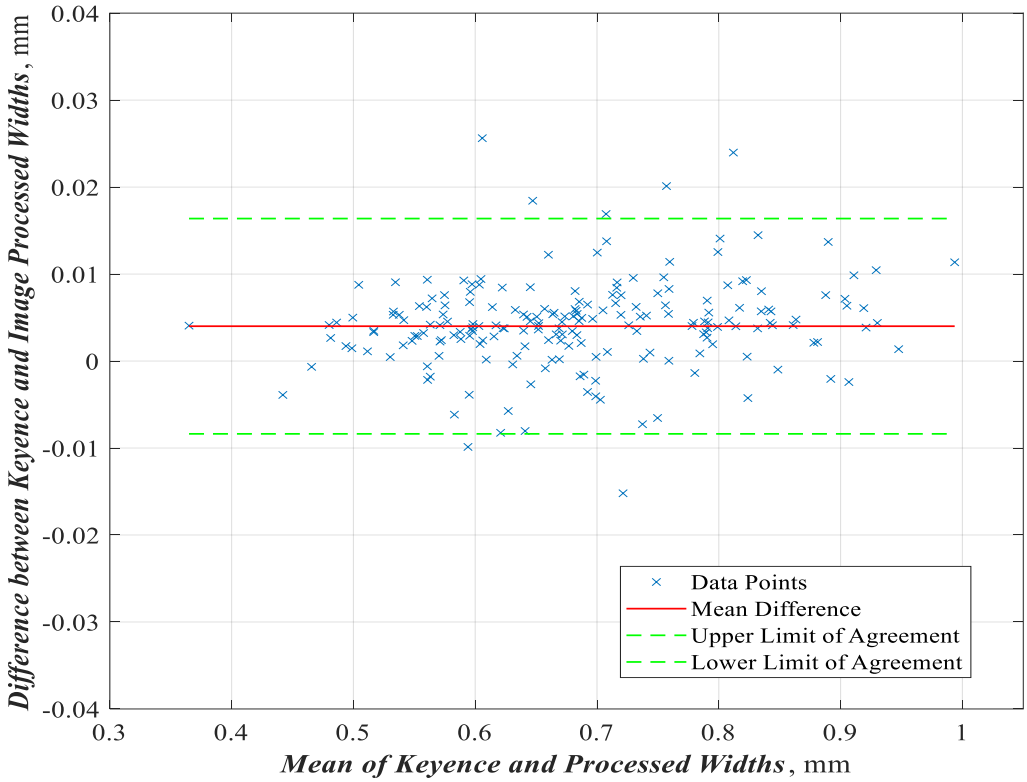

Figure 23: Bland-Altman Plot: Agreement Between Keyence and Processed Line Widths

Upon examining the Bland-Altman plot of Figure 24, it was observed that a bias of $+0.004\ mm$ was introduced in the image processing method. This bias was likely a result of the unidirectional image scanning algorithm encountering yellow dots on the far side of the original detected edge pixels as they were blurred and skewed by the JPEG image compression algorithm towards the lighter side of the fabricated edge, which was the white background of the sample tray. However,

this bias was considered well within reason because the bias introduced only represents 0.59% of the mean line width measured by the Keyence VHX-7000. It is also important to note that only 3.14% of the data in the Bland-Altman Plot fell outside the calculated limits of agreement. This suggests that the measurements found in the image processing procedure are in strong agreement with the Keyence measurements, with only a small proportion of outliers. Furthermore, the maximum difference in the line width measurement between the two measurement techniques was only 3.7% of the mean fabricated line width. Therefore, the reliability and accuracy of the image processing technique in replicating the method established by Keyence was confirmed.

The uncertainty in the processed line width measurement was computed as the standard deviation of the error between the processed line width measurements and the Keyence line width measurements. The uncertainty in the line width data resulting from the image processing algorithm was 0.0063 mm. This uncertainty is 0.92% of the average line width and was considered negligible. The results of the data are discussed in Chapter 4 on Page 48.

3.12 Experimental Design 2: Square Specimen Fabrication

After characterization of fabricated line widths from line fabrication experiments, it was possible to begin experimentation with two-dimensional fabrication. This mode of fabrication requires the consideration of additional parameters, as well as the parameters considered in the line specimen fabrication experiment, to optimally promote intralayer bonding. The experiment considered the effects of increased energy density due to path overlap and the effects of varied scanning path strategies on the formation of defects in fabricated samples.

In the design of this experiment, a square test specimen was selected for fabrication. The square specimen allowed for testing of intralayer junctions such as parallel bonding, T-bonds, X-bonds,

and square corners. The square specimen also allowed for testing of path strategies such as outlining, interlacing, and stitching.

A diagram of the specimen layout on the print bed is shown in Figure 25 below.

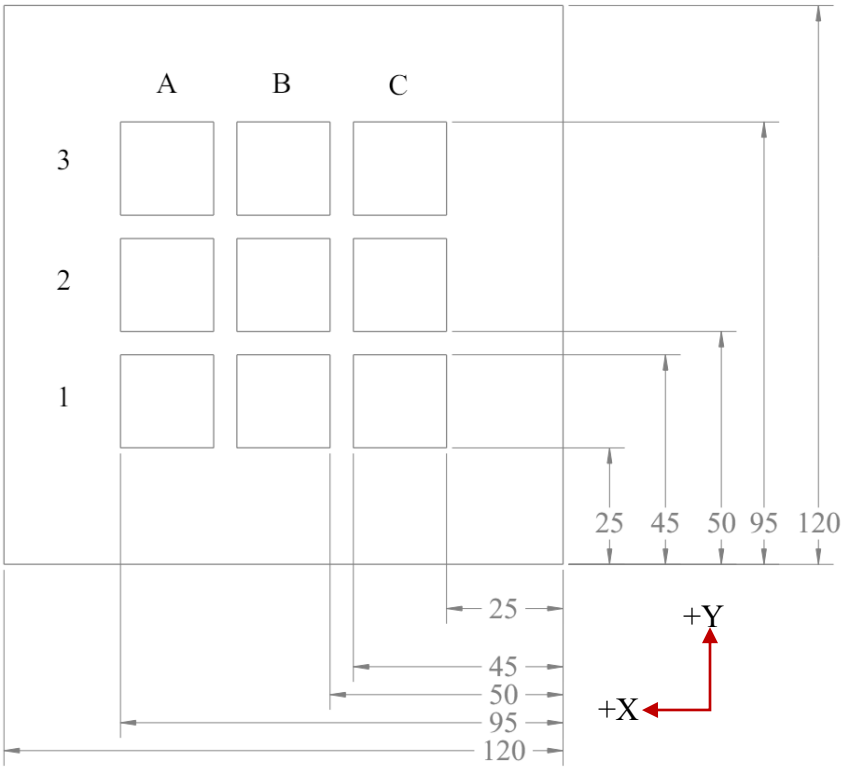

Figure 24: Square Specimen Test Printbed Layout (all dims. in mm.)

To vary print parameters within a single layer, a python GCODE generator script was written. The print parameters of interest in the square specimen, that were made directly configurable during runtime of the script, were the scanning velocity and hatch spacing. The geometry shown in the diagram of Figure 25 was referenced in development of the GCODE script and was maintained throughout experimentation. The generator was modified directly to implement various scanning path strategies.

The alphabetical columns (designated A, B, and C) in Figure 25 were reserved for three set variations of one-dimensional SED for all fabrication runs with values of 0.4 J/mm^2, 0.45 J/mm^2, and 0.50 J/mm^2. The numerical rows (designated 1, 2, and 3) were reserved for three variations of hatch spacing. The variations in scanning path strategy were applied to all specimens within the same fabrication run at a time.

All square specimens were fabricated using the 100% SiC substrate mixture with an average particle diameter of 50 μm.

The machine configuration remained identical to the configuration in the line fabrication experiment. The printing volume was open to standard atmospheric pressure and temperature. Bed adhesion was not implemented.

After running a square specimen fabrication experiment, the samples were removed from the print bed and placed into enclosed sample trays for transportation to optical microscopy. These sample trays were like the trays used in the line fabrication experiment. The 3D-printable tray for hosting and transporting square specimens from the print bed to the microscope is shown in Figure 26 below.

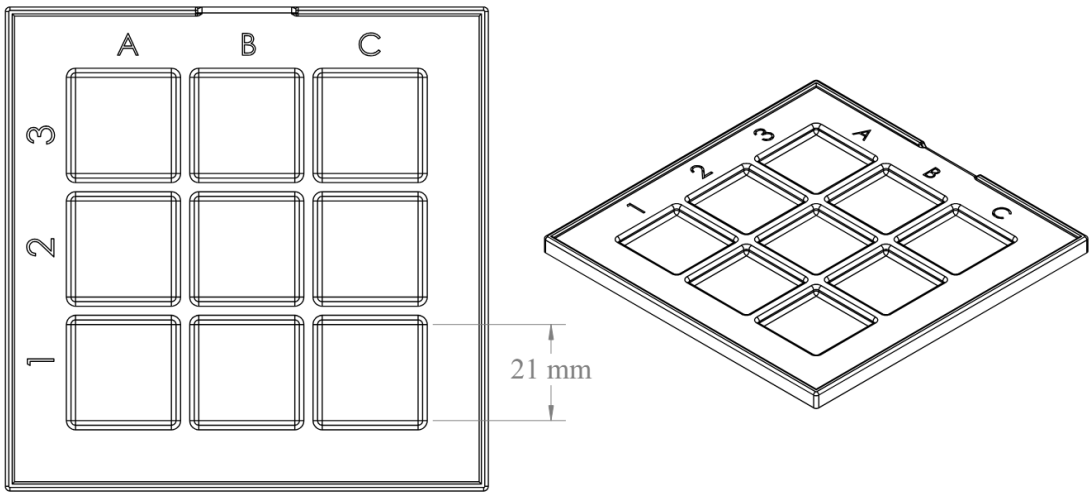

Figure 25: Square Specimen Tray

Additional space was included in the pocket to accommodate for warping.

The square print specimens were inspected using optical microscopy to assess the formation of defects resulting from the machine configuration and the varied process parameters.

Chapter 4: Evaluation of Fabricated Sample Properties

4.1 The Effect of Substrate Mixture and SED on Fabricated Line Widths

To investigate the effect of substrate mixture and SED on fabricated line widths, the data was grouped by concentration of SiC in the substrate. The variations of line widths with respect to the SED for each case of SiC concentration and average grain size of SiO_2 particulate additive were plotted and analyzed. The fabricated line width was normalized with respect to the focal diameter of the laser, H. The results of the fabricated line widths in the substrate with 100% SiC are shown in Figure 27 below.

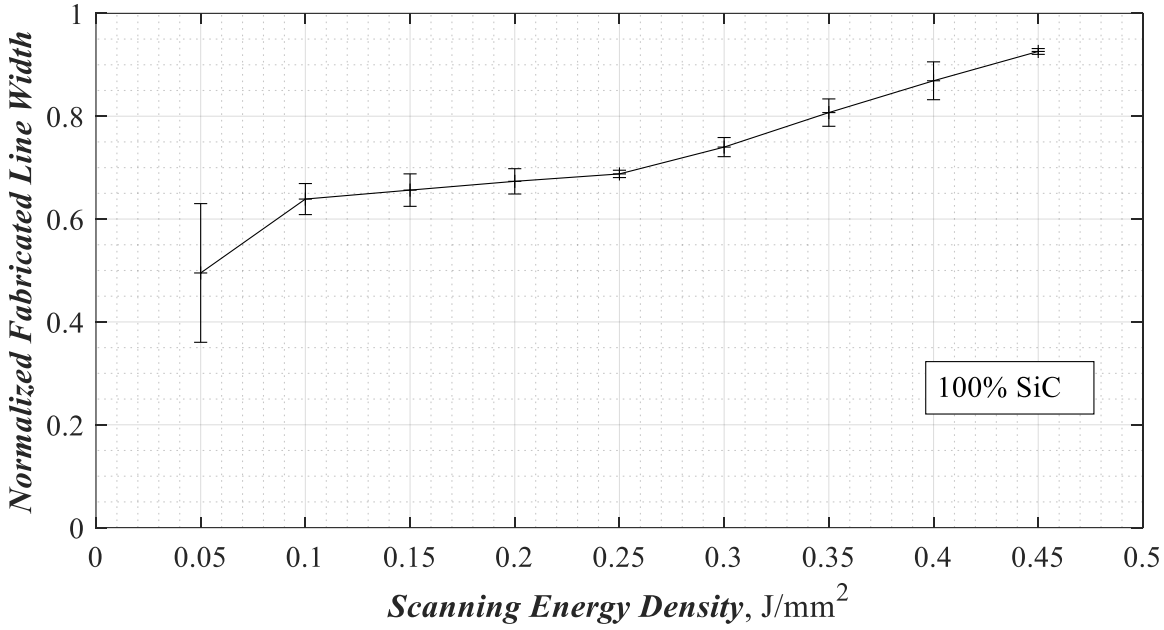

Figure 26: Variation of NFLW with respect to SED in 100% SiC Substrates

The data shown in Figure 27 does not seem to exhibit a linear trend. It is expected that the relationship takes the form of a sigmoid at a broader range of SED. This form would be the result of the melt pool arriving at a thermal equilibrium at a scan velocity of 0 mm/s. The melt pool would reach a maximum diameter as the heat flux from the melt pool to the substrate balances the photothermal flux from the laser beam to the melt pool. At higher scan speeds and lower energy

densities, the melt pool decays into local sintering phenomena. In preliminary testing, scanning velocities greater than 6 mm/s and less than 0.25 mm/s resulted in samples too fragile to transport for further processing. These scanning velocities corresponded to 0.05 J/mm^2 and 0.45 J/mm^2 respectively for the current machine configuration.

Linear regression models were applied to the data to allow provide accuracy in computing the overlap percentage in two-dimensional fabrication experiments. The resulting models should only be considered valid within reasonable bounds of the laser power, focus diameter, powder mixture, recoating method, scanning velocities, and SEDs tested. Variation of any of these parameters independently would result in measurable differences in the results. If SED is maintained, the empirical model could be used as a preliminary model for two-dimensional print testing. The model equation is given below:

$$\forall q \in [0.05, 0.45], \qquad w = \beta_0 + \beta_1 \cdot q \qquad \text{Eq. 5}$$

where w, is the Normalized Fabricated Line Width (NFLW), β_0 is the normalized intercept, β_1 is the slope in mm^2/J, and q is the SED in J/mm^2. The tabulated model parameters are given in Table 3 on page 55.

Note that, as shown in Figure 27, the 100% SiC substrate exhibited lesser average uncertainty in the fabricated line width than the SiC concentrations of the substrates in the following figures. This alluded to increased melt pool stability over a range of SEDs in the 100% SiC substrate mixture. However, at the lowest energy density of 0.05 J/mm^2, the uncertainty was higher than at all other SEDs, and it was observed that the melt pool had drastically destabilized in the lateral mode. This phenomenon was likely caused by the relative heterogeneity, at the scale of the melt pool, in the substrate decreasing due to shrinkage of the melt pool. It was suspected that relatively large volumes of substrate with lower and higher average melting points and thermal conductivities

formed subordinate micro-scale melt pools. If this was the case, these subordinate melt pools influenced the primary melt pool by applying forces due to surface tension and the Marangoni Effect. If this was the case, these forces nonuniformly pulled at the melt pool from all directions.

The results of matching concentrations of SiC substrate were stacked in the plots for brevity and assessment of the effect of SiO_2 additive average grain size on fabricated line width at varied SiC concentrations. These plots are shown in Figures 27-30 below.

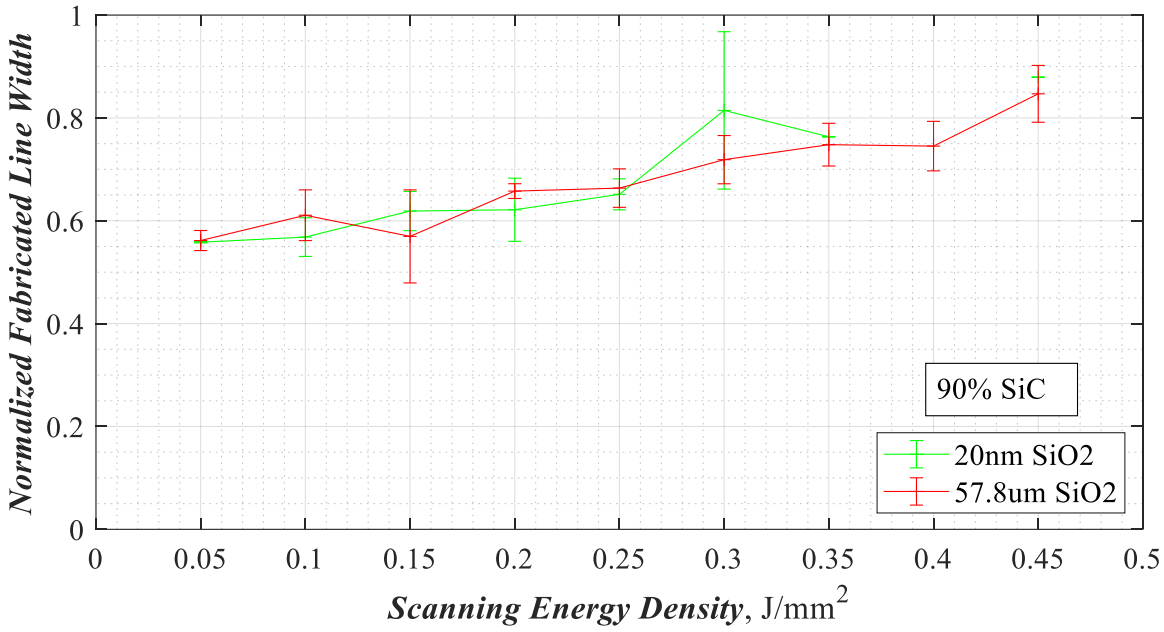

Figure 27: Variation of NFLW with respect to SED in 90% SiC Substrates

Note that in Figure 28, the line width results at energy densities greater than 0.35 J/mm^2 for the substrate containing 20nm SiO_2 are absent. At these higher SEDs, the melt pool exhibited great instability in the "splitting" mode. The melt pool was observed to intermittently split into two adjacent, parallel melt pools and rejoin into a single melt pool in centimeter scale intervals. The reason for this behavior was unknown. Because of this, line width measurements were not taken for this substrate mixture at energy densities higher than 0.35 J/mm^2 except for one specimen which had maintained stability of the melt pool at 0.45 J/mm^2.

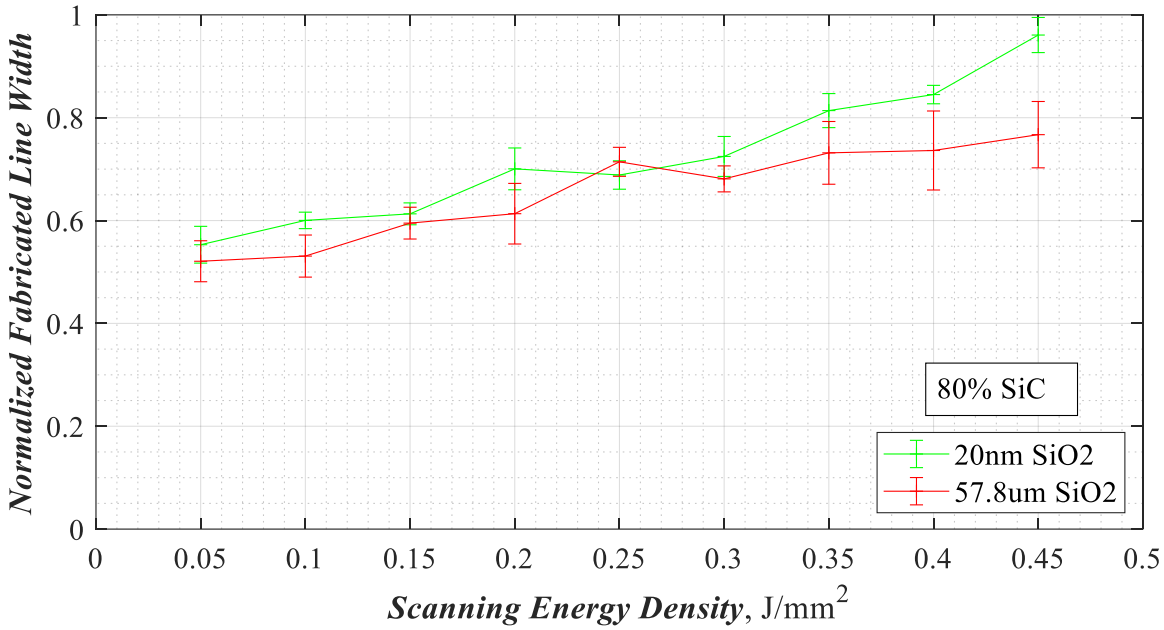

Figure 28: Variation of NFLW with respect to SED in 80% SiC Substrates

Note that in Figure 29, both trends exhibit linear behavior in the tested range of energy densities; however, the substrate with nanoscale SiO_2 particulate inclusion exhibits a noticeably greater rise in line width for each increase in SED than the substrate with microscale SiO_2 particulate inclusion. It was observed that in substrates of 80 vol% SiC, the substrate with nanoscale SiO_2 particulate addition tended to fabricated lines with large agglomerates bonded to the melt pool without full absorption. This observed phenomenon may have been linked to the increased thermal conductivity of the substrate as it was packed more tightly with particulate and partial melting and bonding of substrate, that was not directly scanned, near the melt pool may have occurred.

The results of the fabricated line width measurements in substrates of 70 vol% SiC, the lowest concentration tested with nanoscale SiO_2 particulate additive, are shown in Figure 30 below.

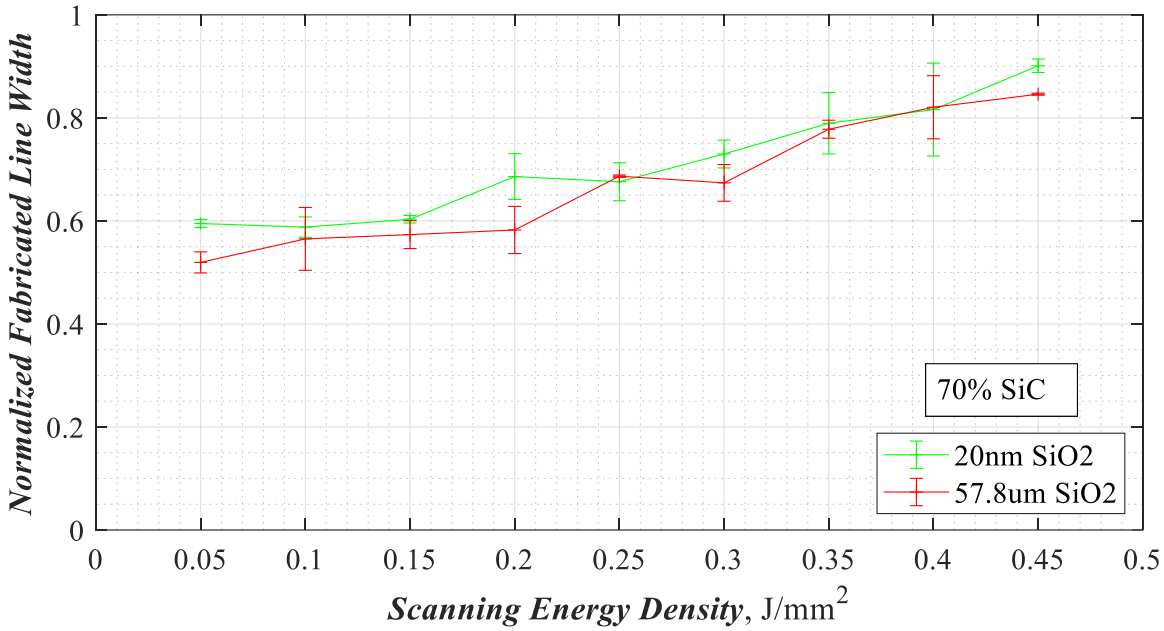

Figure 29: Variation of NFLW with respect to SED in 70% SiC Substrates

It was observed in Figure 30 that the already present agglomeration of the nanoscale SiO_2 particulate had not significantly destabilized the melt pool as the standard deviation in line width between the 70% and 80% SiC substrates did not visibly increase. It is possible that as the packed volume of the nanoscale particulate approached the packed volume of the SiC particulate, the agglomeration of SiO_2 became much more favorable in the mixture.

The results of the fabricated line widths in the substrate with the lowest SiC concentration tested are shown in Figure 31 below.

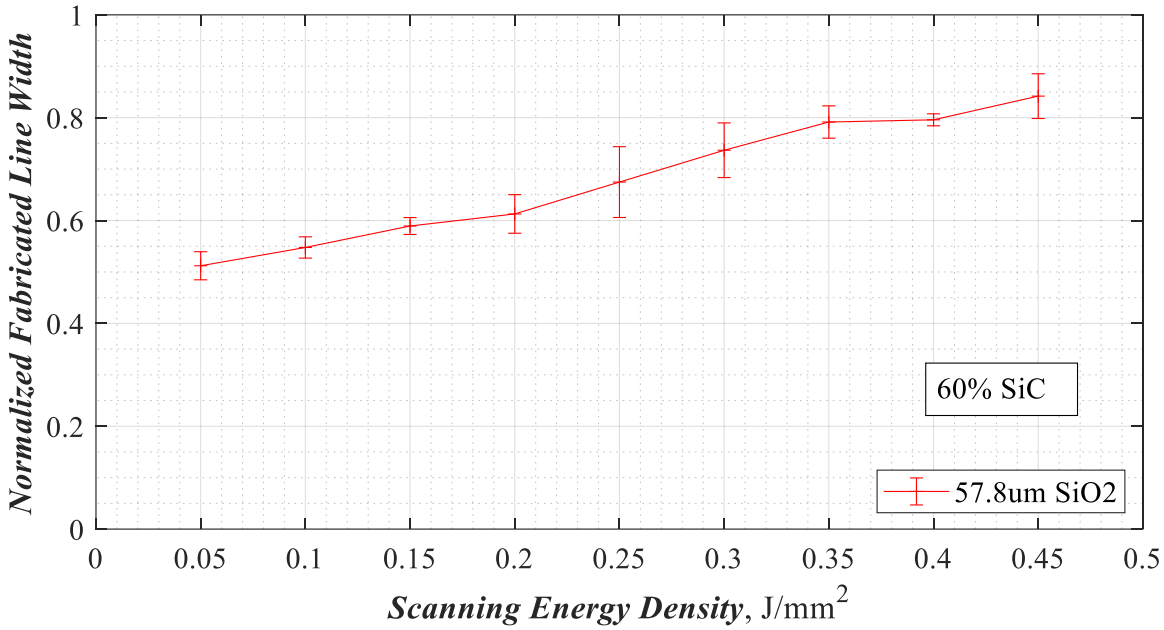

Figure 30: Variation of NFLW with respect to SED in 60% SiC Substrates

Linear models were computed for the above relationships and are summarized with respect to Eq. 5 on Page 49 in Table 3 below.

Table 3: Empirical Model Equations for Predicting Fabricated Line Width Given SED in J/mm²

Substrate Mixture	β_0	β_1 (mm²/J)	R^2
100% SiC	0.490	0.927	0.94
90% SiC, 20nm SiO_2	0.488	0.848	0.90
90% SiC, 58um SiO_2	0.517	0.654	0.92
80% SiC, 20nm SiO_2	0.490	0.930	0.94
80% SiC, 58um SiO_2	0.493	0.647	0.93
70% SiC, 20nm SiO_2	0.516	0.775	0.94
70% SiC, 58um SiO_2	0.457	0.858	0.95
60% SiC, 58um SiO_2	0.462	0.864	0.98

The linear models were grouped by granularity of the SiO_2 additive and plotted with the NFLW results of the substrate containing 100% SiC to visualize the effect of varying substrate SiC concentration. The results of the substrates with 57.8 µm SiO_2 particulate additive are shown on the left, and the substrates with 20 nm SiO_2 particulate additive are shown on the right in Figure 32 below.

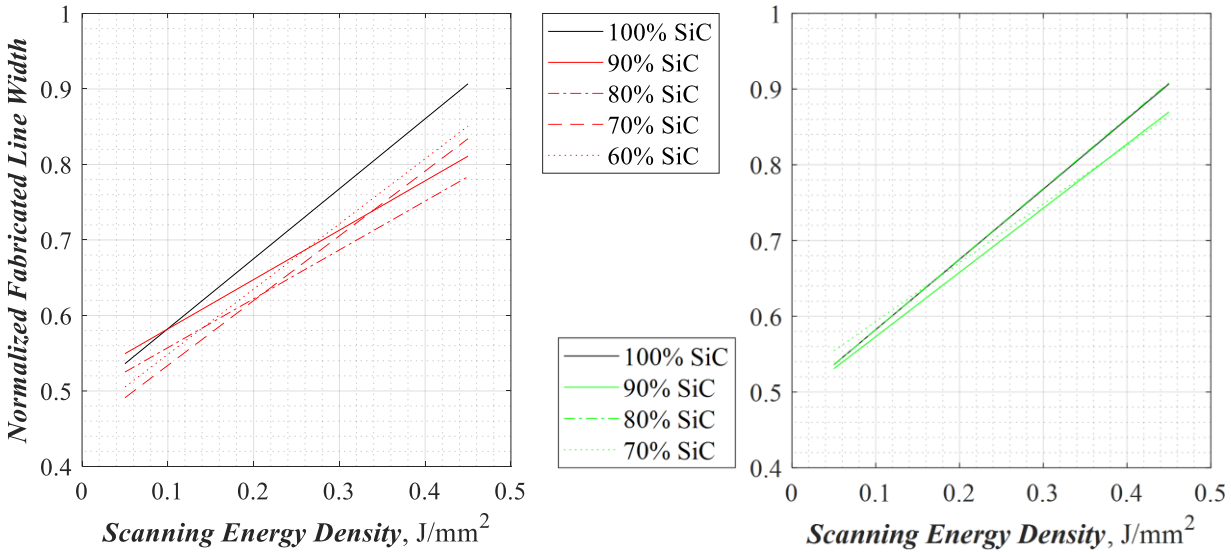

Figure 31: Linear Models of NFLW for Varying Substrate SiC Concentrations Grouped by SiO_2 Additive Granularity: (57.8 µm (Left) and 20 nm (Right))

Note that in Figure 32, the N.F.L.W. axis was shifted and scaled relative to previous figures to clarify the differences in the models for each case. From the figures and the parameters tabulated in Table 3 it is evident that inclusion of SiO_2 particulate in the substrate mixture generally decreases the fabricated line width. Although the fabricated line width decreases, this does not assert that the quality of the fabricated line had decreased. Fabrication quality is discussed beginning on page 58.

To investigate the overall effect of nanoscale and microscale SiO_2 inclusion, in the microscale SiC substrate, on the fabricated line width, all the measurement data for each substrate mixture case

was grouped by average particulate diameter of the SiO_2 additive. Linear regressions were fitted to the data for comparison. These data are shown in Figure 33 below.

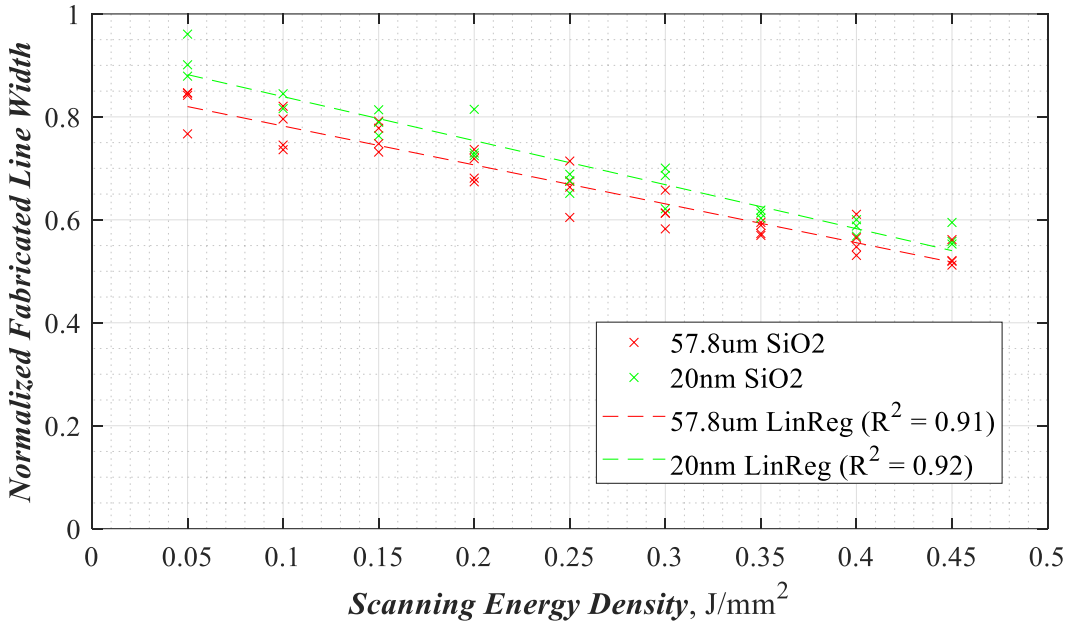

Figure 32: NFLW Variation w.r.t. S.E.D. with SiC Concentrations Grouped and SiO_2 Granularity Ungrouped

Figure 33 shows that the inclusion of nanoscale SiO_2 particulate increased the fabricated line width at lower SEDs by nearly 5%, however, the effect diminished as SED increased. It was suspected that as the SED increased, the primary melt pool began to absorb the SiO_2 agglomerations discussed below Figure 29.

The results of the substrate mixture and SED variation experiment provided key insights into the effect of these process parameters on the widths of the fabricated lines. To make decisions about what substrate mixtures and SEDs were to be utilized in the experimentation on fabrication of square samples, it was also pertinent to assess at what values these process parameters were optimized for fabricating line uniformity.

4.2 The Effect of Substrate Mixture and SED on Fabricated Line Uniformity

The edge contour variation, or smoothness, of the edges of the fabricated lines is related to the homogeneity of the substrate and, more importantly, the stability of the scanning melt pool. Statistical measures of the residuals of the detected edge points relative to the linear regression used to define the edge locations are useful in assessing the uniformity of the fabricated lines.

The Root Mean Square Error (RMSE) of the residuals can provide insight into the uniformity of the fabricated lines. In the context of edge uniformity, a lower RMSE value indicates that the detected edges closely align with the ideal or expected edge positions, reflecting high precision and uniformity

The RMSE of the residuals of the detected points relative to the linear regression of the detected edge were computed and averaged for each value of SED. Each substrate mixture was grouped, and the data were plotted. The results of this analysis are shown in Figure 34 below. Note that the substrates with nanoscale SiO_2 particulate additive are shown in green hues The substrates with microscale SiO_2 particulate are shown in red hues.

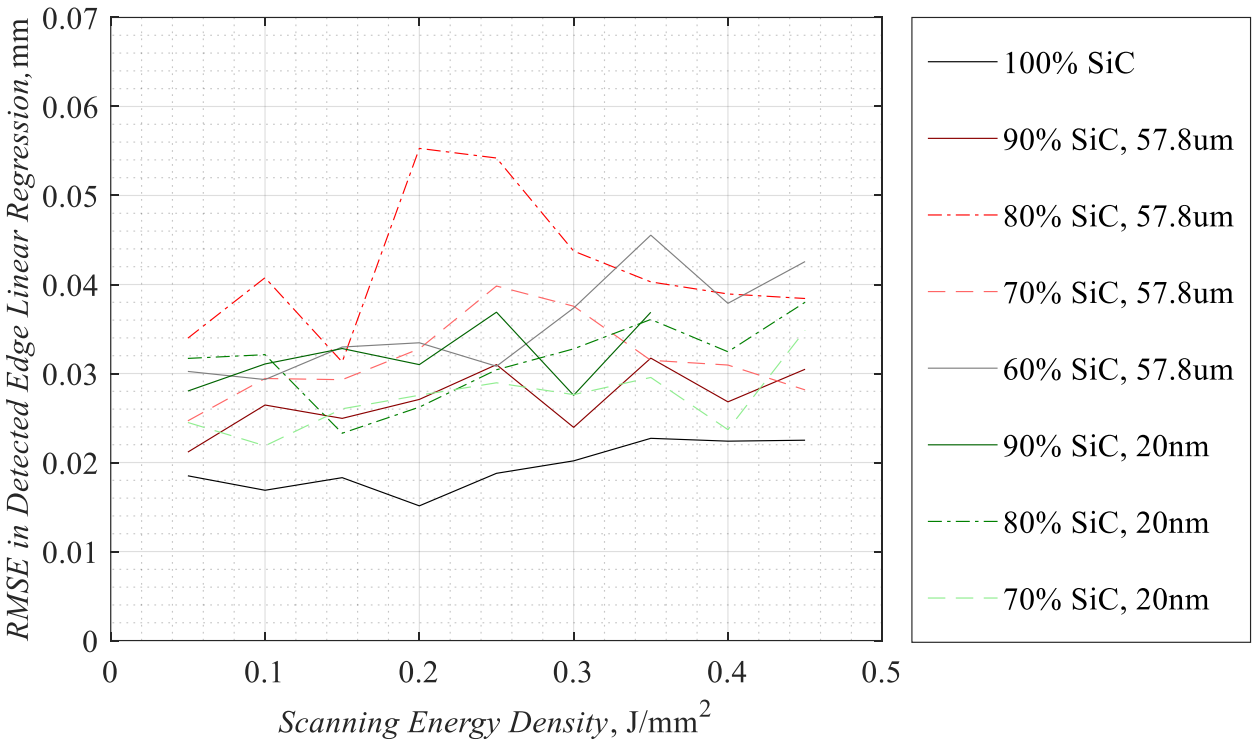

Figure 33: Variation of RMSE in Detected Edge Linear Regression w.r.t. SED

Figure 34 shows that the average RMSE's, across the domain of SEDs tested, falls within 0.015 and 0.055 mm. The maximum average RMSE appears in the 80% SiC, 57.8μm substrate. This average RMSE equates to 12.7% of the lowest line width measured in the corresponding case. The 100% SiC concentration substrate mixture exhibited the lowest average RMSE of all tested substrate mixtures across the range of SEDs tested, which was attributed to the fabricated lines having the lowest surface roughness and irregularity.

A trend was apparent in Figure 34 that described an increase in average RMSE as SED increased. This corresponded to a decrease in fabricated uniformity with increased SED. This trend could be explained by an increase in chemical reactions in the melt pool due to the increased melt pool temperature incurred by the increased SED. The trend could also be explained by the bonding of sintered agglomerates to the primary melt pool at increased melt pool temperatures because the increased temperature contributes to increased local sintering of the substrate surrounding the melt

pool. These locally sintered agglomerates had greater irregularity due to the agglomerating forces caused by the Marangoni effect being negligible in the absence of melt pool formation. It was also possible that at lower scanning velocities (higher SEDs) the variation in the laser control error increased in magnitude due to the length and timing of the steps in the stepper motors driving the gantry-mounted laser.

The results of this analysis provided key insights into the effect of SED and substrate mixture on the irregularity/uniformity of the fabricated lines. With these insights, the value of pure and homogenous substrates, fine laser beam control, and environmental control were realized. These parameters should be investigated to form a more complete understanding of the uniformity of parts fabricated by SLM of SiC/SiO_2 substrates.

4.3 Defect Formation in Fabricated Square Specimens

The formations of defects as results of suboptimal process parameters in square specimen fabrication were investigated. The results of this analysis remain largely qualitative. The analysis focused on the appearance of success in attempts to perform intralayer bonding of joints and corners. Parallel, T, and cross joints bonding were demonstrated in this experiment. Square corner fabrication was also demonstrated. An image from optical microscopy showing parallel bonding of 100% SiC substrate is shown in Figure 35 below.

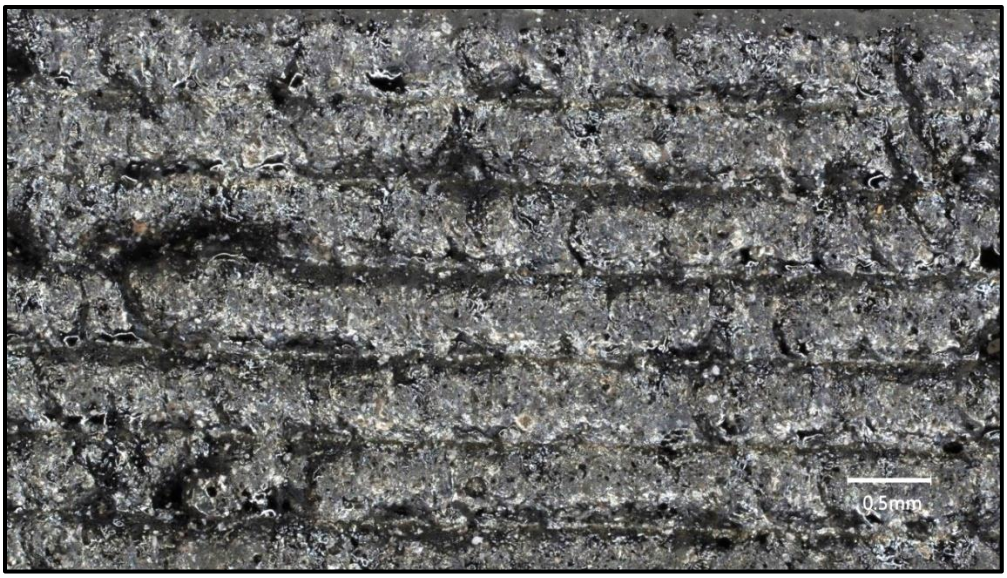

Figure 34: Optical Image of General Parallel Bonding in SiC Square Specimen

Figure 35 shows a section of a fabricated square sample printed with 0.45 mm hatch spacing, and a one-dimensional SED of 0.35 J/mm^2. This specimen demonstrated success in fabricating parallel bonds. Irregular pores of 200 microns in length were observed in the sample. However, this image shows promise for the SLM of SiC substrates.

A depth chart of the parallel bonding region was created using a Keyence VHX-7000 Optical Microscope to demonstrate the nature of parallel bonding in SiC substrates. This graph is shown in Figure 36 below.

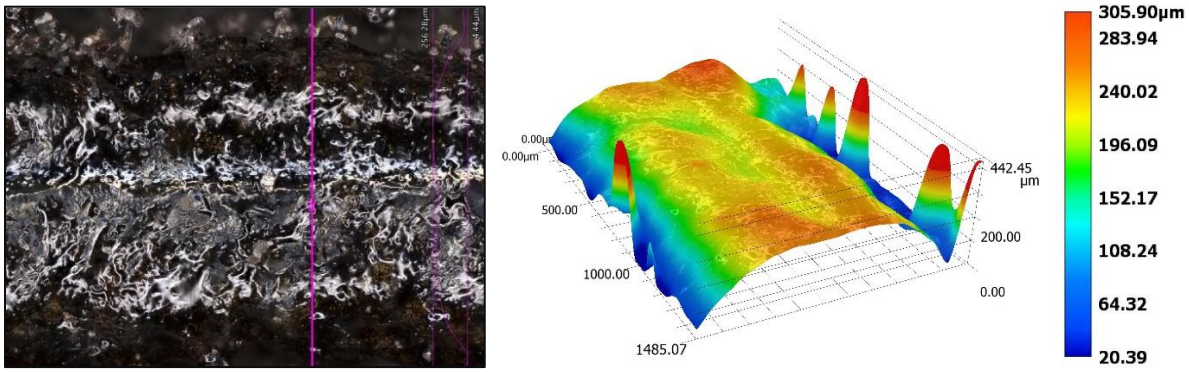

Figure 35: Depth Chart of Parallel Bond Region in SiC Specimen

In Figure 36, the blending of two parallel melt pools can be observed. The maximum difference in the highest peak and lowest valley in the scanned region was on the order of 100 microns. With an average particle diameter of 50 microns, the maximum variation in the surface height was on the order of a few substrate particles. With an increase in substrate purity and laser control precision it would be possible to create layers with sufficient uniformity for recoating.

T-Bonds were fabricated at the perimeter of the square specimens where a square outline was first fabricated. An example of T-Bonding is shown in Figure 37 below.

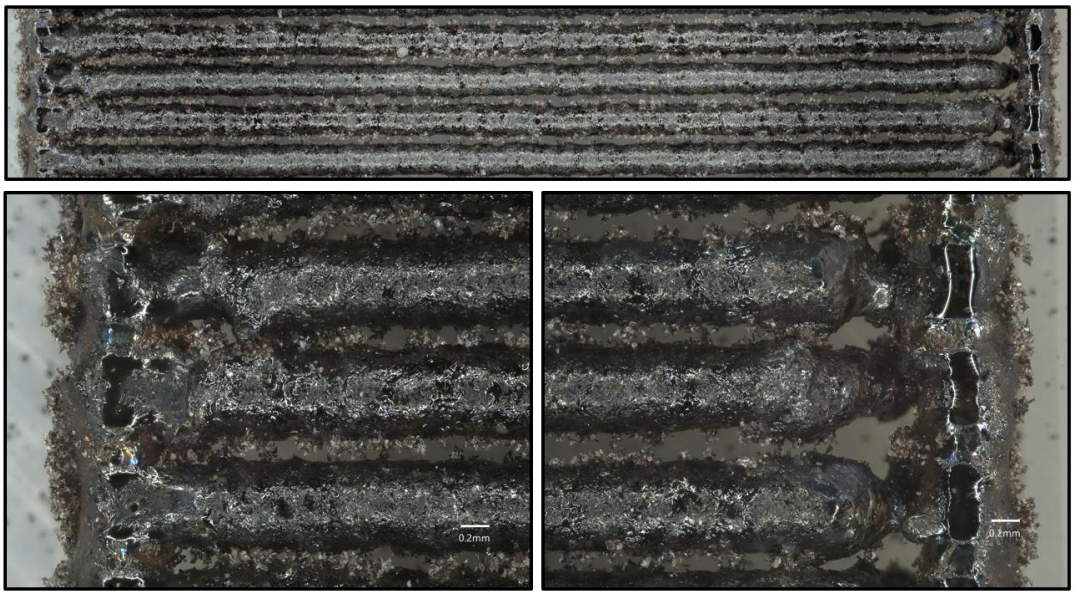

Figure 36: Optical Images of General T-Joint Bonding in SiC Square Specimen

The T-Joint bonds in Figure 37 were fabricated by first scanning a square outline and subsequently scanning from the centerline of the maximum X edge to the centerline of the minimum X edge without translation in the Y direction. It was found that more energy was required for melt pool formation on previously scanned sections. A dwell of at least 500 ms, corresponding to 2.5 J emitted by the laser, at the start of the spanning scan was required to achieve T-Bonding. Dwelling, stitching, slowing, passing strategies, and combinations of all the above were tested to form a

smooth T-Bond at the end of the spanning scan. However, a smooth T-Bond at end of the spanning scan was never achieved. The most probable cause of this defect was warping of the outline during the scan of the outline. The outline scan was performed in a counterclockwise fashion, starting at the maximum X and minimum Y corner. At each corner, the laser was turned off to allow the melt pool to solidify, and then the melt pool was reformed to begin the scan of the next edge. This was done to mitigate the effect of thermal warping in the absence of bed adhesion. The primary reason for the failure to produce a smooth T-Bond at the end of the spanning scan was suspected to be a relocation of the outline edge during the scanning of the outline. The translation of the outline edge occurred due to thermal warping still present with the modified corner scanning strategy. As the scanned line translated, it also swept the powder substrate, forming a substrate void near the outline. This was not observed at the start of the spanning scan, which was attached to the last edge scanned in formation of the outline. At this location, no observable thermal warping had occurred during formation of the outline; therefore, a significant substrate void was not present. It is suspected that incorporation of bed adhesion would help to mitigate thermal warping.

Cross-joint bonds were fabricated by extension of the spanning scans. An example of cross-joint bonding is shown in Figure 38 below.

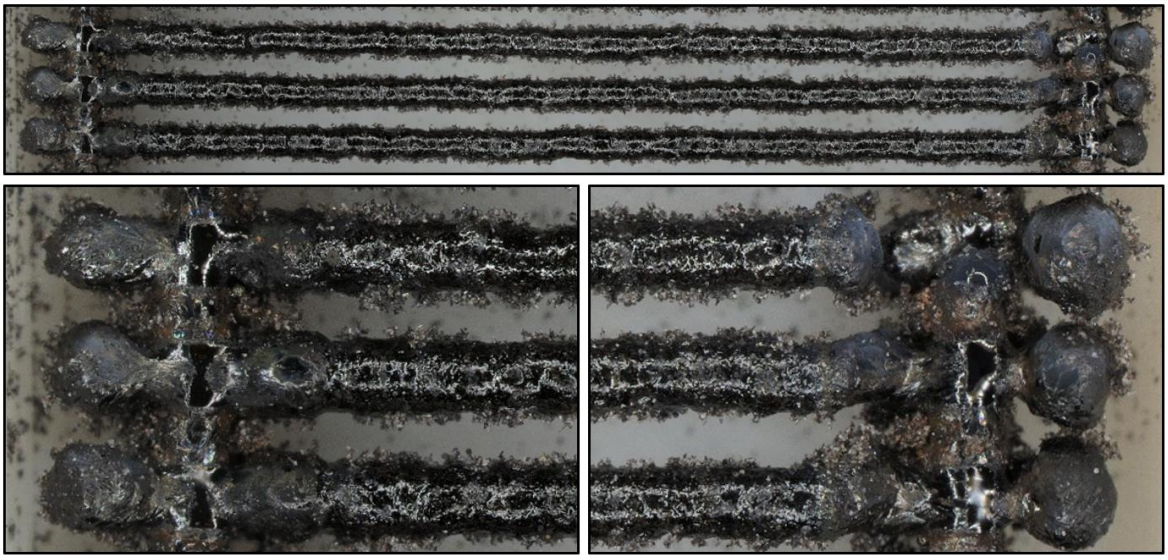

Figure 37: Optical Images of General Cross-Joint Bonding in SiC Square Specimen

The cross-joint bonds shown in Figure 38 were fabricated by incorporation of dwells and decelerated scans perpendicularly crossing the square outline. These strategies energized the melt pool to higher temperatures to enable melting and bonding of the previously scanned locations. Similar issues in bonding of the ends of the spanning scan as discussed below Figure 37 were observed. It was also observed that the variation of energy density produced visible changes in the color of the solidified surface of the part. The success of the cross-joints at the start of the spanning scan relative to the failures of cross-joints at the end of the scan confirmed that the primary reason for failures in the T-Joints is not a result of suboptimal scanning strategy, lagging melt pool, or absence of preheating of the joint location. Instead, this phenomenon was a result of uncontrolled thermal warping.

Also, merging of the melt pool with previously scanned parallel, adjacent structures was observed. An example of this phenomenon is shown in Figure 39 below.

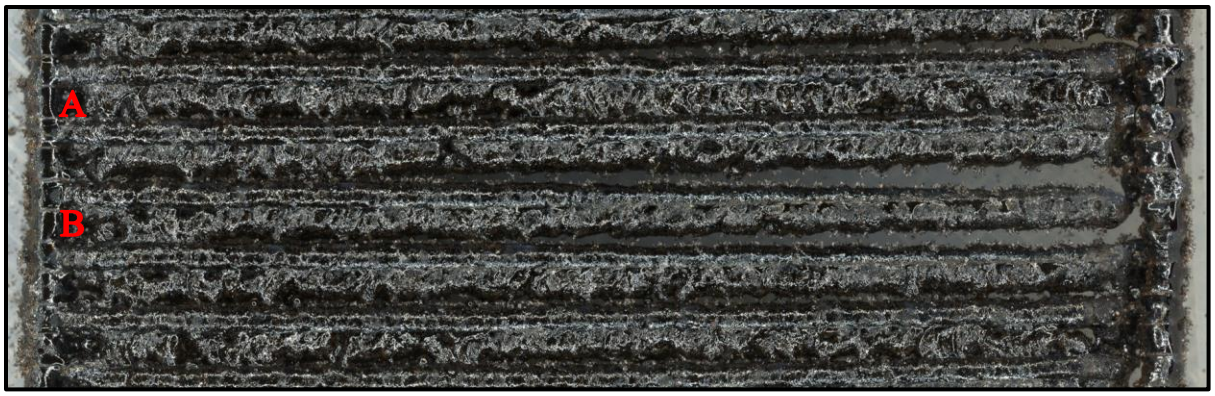

Figure 38: Optical Image of Parrel Bonding Merge Defect

It was observed that in layers using interlaced scanning strategies, unstable melt pools would often merge with the previously scanned, parallel, and adjacent spanning structure. This phenomenon was made worse with unsuccessful bonding of the primary pass structure with the outline structure, as shown along line B in the figure. This phenomenon was called affinity merging. It was likely due to the deformation of the structure, formed by the primary pass, as a result of thermal warping during the secondary pass. It was observed that secondary passes would often begin with no affinity to either side of the parallel, adjacent, primary pass structures, but the melt pool would often merge at some point along the length of the scan. This phenomenon was difficult to control, as evidenced by the differences in line A and line B in Figure 39 above which were scanned with identical process parameters.

Attempts to mitigate the affinity merging by maintaining a one-dimensional SED of 0.45 J/mm^2 and a decrease of hatch spacing down to 0.25 mm resulted in runaway thermal stresses that caused the specimen to catastrophically warp and crack. An example of this phenomenon is shown in Figure 40.

Figure 39: Optical Image of Warped and Cracked SiC Square Specimen

It was observed that with the current machine configuration it was not possible to eliminate affinity merging before large cracks formed due to increased thermally induced stresses. At these elevated, two-dimensional SEDs, millimeter scale voids were observed. These voids may have been an artifact of dramatically increased sublimation in the melt pool, that would have caused the formation of gaseous bubbles. Because this phenomenon was not generally observed at lower two-dimensional SEDs, this may have been the point where the subversion of sublimation terminated.

The most consistent square specimen fabricated is shown in Figure 41 below.

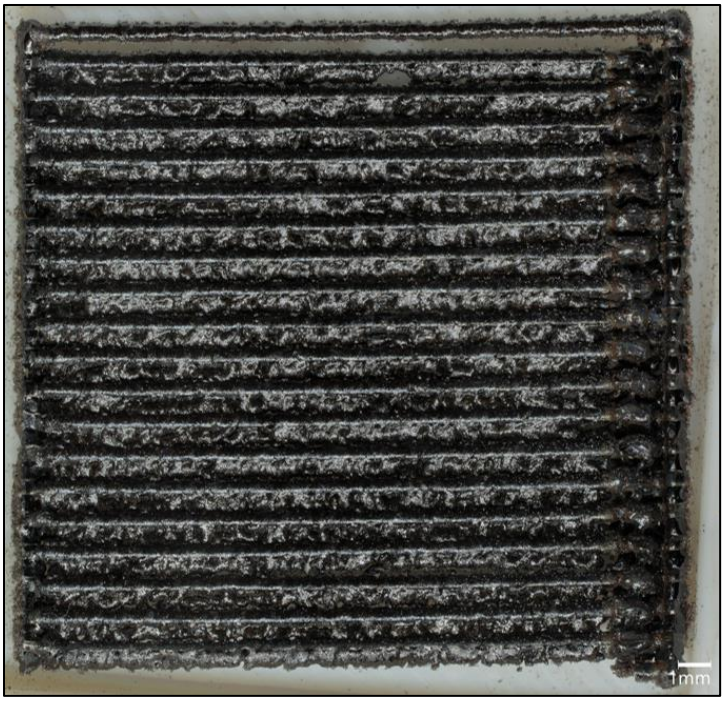

Figure 40: Optical Image of the Square SiC Specimen of Highest Consistency

The square specimen in Figure 41 was fabricated using a one-dimensional SED of 0.45 J/mm^2 and a hatch spacing of 0.40 mm. This was equivalent to a two-dimensional SED of 1.125 J/mm^2. The parallel scans were uniformly bonded throughout the sample. It was observed that the end of the spanning scan path (right) was less uniform than the start (left). This was a result of attempts to optimize the scanning strategy to achieve T-Joint bonding at the end of the spanning scan.

The results of the square specimen fabrication test showed that parallel bonding, T-Joint bonding, and cross-joint bonding is possible in SLM of SiC substrates. It also revealed that careful control of the process parameters are necessary to increase stability and repeatability of the fabrication process.

Chapter 5: Conclusions and Future Work

5.1 Conclusions on SLM of Silicon Based Ceramics

Investigations on SLM of SiC substrates concluded that it is possible to perform SLM on SiC substrates. It is unknown if the resulting fabrications were composed of homogenized SiC crystals or were a complex composite of SiC, SiO_2, Si, and C.

It was shown that substrates prepared with SiO_2 additives generally resulted in a decrease of fabricated line width and a decrease in fabricated line uniformity. The reasons for the observed trends are complex and multifaceted as they involve classical chemical, thermal, and physical phenomena as well as case specific phenomena.

It was shown that parallel, T-joint, cross-joint, and corner bonding is possible in SiC substrates, but an aggressive approach to controlling process parameters is necessary to fabricate three-dimensional parts using SiC substrates.

5.2 Recommendations for Future Work

The machine demonstrated that it could perform SLM; however, it lacks many of the standard features in modern SLM machines. Without bed adhesion, a controlled chamber, optical mechanisms for beam control, chemical-grade substrates, a CO2 laser, or a fiber optic laser, SLM of SiC-based substrates was challenging.

The first recommendation for future work is to analyze the chemical composition of fabricated samples. This could be done using X-Ray Diffraction technology. The results of this analysis would be conclusive in determining if subversion of sublimation in SiC is possible by using SLM processes.

Secondly, it is necessary to incorporate bed adhesion in the process. The absence of bed adhesion was the primary bottleneck in moving forward towards fabrication of three-dimensional parts. Bed adhesion may be possible using a brick or bricks of SiC fixed to the existing build plate by a light-duty adhesive. Industrially prepared sharpening stones and grinding wheels are often constructed using hot-pressed, sintered SiC and could work well as an initial build plate.

The third recommendation for future work is to source chemical grade SiC powder. It is possible that the lower grade powder used in experimentation contributed to the formation of defects and irregularities in the fabricated samples. It may also be beneficial to iterate on the roller-pusher recoater to compact the substrate. A vibrating module or tamping device could also be used for substrate compaction, but careful control of the compaction is necessary to ensure that the focal length of the laser is accounted for as intense compaction would significantly vary the height of the substrate.

In terms of printer modifications, another recommendation is to upgrade the gantry to support dual drive in the Y-Axis. This can be accomplished using a single, dual-shaft stepper motor and idler pulleys. The X-Axis carriage should also be upgraded to use a linear slide rail instead of an 8020-extrusion carriage. These upgrades would directly increase the precision of the gantry system and indirectly increase the stability of the melt pool.

The fifth recommendation for future work is to upgrade the laser print-head to a more powerful laser. Higher power lasers, relative to the 5W laser used in these experiments, can be implemented for some monetary and time-wise cost. However, a more powerful laser would necessitate a shielded build chamber. If a shielded build chamber is to be constructed, it would be beneficial to pressure seal it for incorporation of an inert gas environment. Temperature control of the chamber and an inert environment would reduce oxidation of the melt pool. A build chamber under vacuum

could reduce porosity but also may increase sublimation in the melt pool. An inert gas environment would come at less cost because the air can be purged satisfactorily without a perfect seal.

In conclusion, an SLM machine was constructed, and SLM of SiC substrates was demonstrated. It is possible that SiC was not present in the fabricated samples; instead, they were formed of SiO_2, C, and Si. However, a sudden, dramatic increase in millimeter-scale porosity at slightly elevated SEDs indicates that gas production and sublimation may have been subverted with optimal process parameters. Work remains to stabilize the melt pool and reduce environmental perturbations.

Bibliography

[1] La Via, F., Alquier, D., Giannazzo, F., Kimoto, T., Neudeck, P., Ou, H., Roncaglia, A., Saddow, S. E., and Tudisco, S., 2023, "Emerging SiC Applications beyond Power Electronic Devices," Micromachines, **14**(6), p. 1200.

[2] Ruys, A. J., 2023, *Silicon Carbide Ceramics: Structure, Properties and Manufacturing*, Elsevier.

[3] Smith, T. P., and Davis, R. F., 2001, "Silicon Carbide," *Encyclopedia of Materials: Science and Technology*, K.H.J. Buschow, R.W. Cahn, M.C. Flemings, B. Ilschner, E.J. Kramer, S. Mahajan, and P. Veyssière, eds., Elsevier, Oxford, pp. 1–6.

[4] Wang, X., Gao, X., Zhang, Z., Cheng, L., Ma, H., and Yang, W., 2021, "Advances in Modifications and High-Temperature Applications of Silicon Carbide Ceramic Matrix Composites in Aerospace: A Focused Review," Journal of the European Ceramic Society, **41**(9), pp. 4671–4688.

[5] Kimoto, T., and Cooper, J. A., 2014, *Fundamentals of Silicon Carbide Technology: Growth, Characterization, Devices and Applications*, John Wiley & Sons.

[6] Flörke, O. W., Graetsch, H. A., Brunk, F., Benda, L., Paschen, S., Bergna, H. E., Roberts, W. O., Welsh, W. A., Libanati, C., Ettlinger, M., Kerner, D., Maier, M., Meon, W., Schmoll, R., Gies, H., and Schiffmann, D., 2008, "Silica," *Ullmann's Encyclopedia of Industrial Chemistry*, John Wiley & Sons, Ltd.

[7] Heaney, P. J., Prewitt, C. T., Gibbs, G. V., and Mineralogical Society of America, 1994, *Silica: Physical Behavior, Geochemistry and Materials Applications / Editors P.J. Heaney, C.T. Prewitt, G.V. Gibbs.*, Mineralogical Society of America, Washington, D.C.

[8] Vasilos, T., Ertürk, T., and Ambati, R., 1993, "SCS-6 SiC Fiber Reinforced Fused Silica Composites," *Proceedings of the 17th Annual Conference on Composites and Advanced Ceramic Materials: Ceramic Engineering and Science Proceedings*, John Wiley & Sons, Ltd, pp. 955–962.

[9] Lee, H.-Y., Tsui, F.-C., and Lee, Y.-C., 2019, "Structural and Microstructural Studies on SiC-SiO2 Ceramic Composites," Materials Chemistry and Physics, **233**, pp. 203–212.

[10] Li, T., Zhang, Y., Zhang, J., Fu, Y., and Li, J., 2021, "Improved Antioxidative and Mechanical Properties of SiC Coated C/C Composites via a SiO2-SiC Reticulated Layer," Journal of the European Ceramic Society, **41**(13), pp. 6151–6159.

[11] Kelly, J. F., Fisher, G. R., and Barnes, P., 2005, "Correlation between Layer Thickness and Periodicity of Long Polytypes in Silicon Carbide," Materials Research Bulletin, **40**(2), pp. 249–255.

[12] Berzelius, J. J., 1824, Ann. Phys. Chem., **1**(169).

[13] Acheson, E. G., 1893, "US492767A."

[14] Harris, G. L., Harris, G. L., and Institution of Electrical Engineers, eds., 1995, *Properties of Silicon Carbide*, INSPEC, the Inst. of Electrical Engineers, London.

[15] Byrappa, K., and Yoshimura, M., 2008, *Handbook of Hydrothermal Technology*, Cambridge University Press.

[16] Ji, R., Liu, Y., Zhang, Y., Cai, B., Li, H., and Ma, J., 2010, "Optimizing Machining Parameters of Silicon Carbide Ceramics with ED Milling and Mechanical Grinding Combined Process," Int J Adv Manuf Technol, **51**(1), pp. 195–204.

[17] Genna, S., Menna, E., Rubino, G., and Trovalusci, F., 2023, “Laser Machining of Silicon Carbide: Experimental Analysis and Multiobjective Optimization,” Ceramics International, **49**(7), pp. 10682–10691.
[18] Calignano, F., Manfredi, D., Ambrosio, E. P., Biamino, S., Lombardi, M., Atzeni, E., Salmi, A., Minetola, P., Iuliano, L., and Fino, P., 2017, “Overview on Additive Manufacturing Technologies,” Proceedings of the IEEE, **105**(4), pp. 593–612.
[19] Grossin, D., Montón, A., Navarrete-Segado, P., Özmen, E., Urruth, G., Maury, F., Maury, D., Frances, C., Tourbin, M., Lenormand, P., and Bertrand, G., 2021, “A Review of Additive Manufacturing of Ceramics by Powder Bed Selective Laser Processing (Sintering / Melting): Calcium Phosphate, Silicon Carbide, Zirconia, Alumina, and Their Composites,” Open Ceramics, **5**, p. 100073.
[20] Zhao, X., and Wang, T., 2023, “Laser Powder Bed Fusion of Powder Material: A Review,” 3D Printing and Additive Manufacturing, **10**(6), pp. 1439–1454.
[21] Wang, J., Zhu, R., Liu, Y., and Zhang, L., 2023, “Understanding Melt Pool Characteristics in Laser Powder Bed Fusion: An Overview of Single- and Multi-Track Melt Pools for Process Optimization,” Advanced Powder Materials, **2**(4), p. 100137.
[22] Tagliaferri, V., Trovalusci, F., Guarino, S., and Venettacci, S., 2019, “Environmental and Economic Analysis of FDM, SLS and MJF Additive Manufacturing Technologies,” Materials, **12**(24), p. 4161.
[23] “Laser Energy Density - an Overview | ScienceDirect Topics” [Online]. Available: https://www.sciencedirect.com/topics/engineering/laser-energy-density. [Accessed: 13-Jun-2024].
[24] Kurzynowski, T., Stopyra, W., Gruber, K., Ziółkowski, G., Kuźnicka, B., and Chlebus, E., 2019, “Effect of Scanning and Support Strategies on Relative Density of SLM-Ed H13 Steel in Relation to Specimen Size,” Materials, **12**(2), p. 239.
[25] Ji, X., Li, S., Liu, H., Li, X., Zhang, X., Liu, L., Li, S., Gao, L., Wang, S., Chen, B., and Li, Y., 2024, “Process Optimization of SiC-Reinforced Aluminum Matrix Composites Prepared Using Laser Powder Bed Fusion and the Effect of Particle Morphology on Performance,” Materials, **17**(5), p. 1187.
[26] Larimian, T., Kannan, M., Grzesiak, D., AlMangour, B., and Borkar, T., 2020, “Effect of Energy Density and Scanning Strategy on Densification, Microstructure and Mechanical Properties of 316L Stainless Steel Processed via Selective Laser Melting,” Materials Science and Engineering: A, **770**, p. 138455.
[27] Guo, M., Gu, D., Xi, L., Zhang, H., Zhang, J., Yang, J., and Wang, R., 2019, “Selective Laser Melting Additive Manufacturing of Pure Tungsten: Role of Volumetric Energy Density on Densification, Microstructure and Mechanical Properties,” International Journal of Refractory Metals and Hard Materials, **84**, p. 105025.
[28] Monton Zarazaga, A., 2021, “Additive Manufacturing of Silicon Carbide-Based Ceramics by Powder Bed Selective Laser Processing : From the Functionalized Powder to the Final Part,” phd.
[29] Meyers, S., De Leersnijder, L., Vleugels, J., and Kruth, J.-P., 2018, “Direct Laser Sintering of Reaction Bonded Silicon Carbide with Low Residual Silicon Content,” Journal of the European Ceramic Society, **38**(11), pp. 3709–3717.
[30] Meyers, S., Leersnijder, L. D., Vleugels, J., and Kruth, J.-P., 2018, “Increasing the Silicon Carbide Content in Laser Sintered Reaction Bonded Silicon Carbide,” *Processing, Properties, and Design of Advanced Ceramics and Composites II*, John Wiley & Sons, Ltd, pp. 207–215.

[31] “Additive Manufacturing of Technical Ceramics: Laser Sintering of Alumina and Silicon Carbide - KU Leuven” [Online]. Available: https://kuleuven.limo.libis.be/discovery/fulldisplay/lirias2818105/32KUL_KUL:Lirias. [Accessed: 11-Jun-2024].
[32] 2024, “Klipper3d/Klipper.”
[33] Montón Zarazaga, A., Abdelmoula, M., Küçüktürk, G., Maury, F., Ferrato, M., and Grossin, D., 2022, “Process Parameters Investigation for Direct Powder Bed Selective Laser Processing of Silicon Carbide Parts,” Prog Addit Manuf, **7**(6), pp. 1307–1322.
[34] Kozak, J., Zakrzewski, T., Witt, M., and Dębowska-Wąsak, M., 2021, “Selected Problems of Additive Manufacturing Using SLS/SLM Processes,” Transactions on Aerospace Research, **2021**(1), pp. 24–44.
[35] Yao, W., Guangsheng, G., Fei, W., and Jun, W., 2002, “Fluidization and Agglomerate Structure of SiO2 Nanoparticles,” Powder Technology, **124**(1), pp. 152–159.
[36] Martin Bland, J., and Altman, DouglasG., 1986, “STATISTICAL METHODS FOR ASSESSING AGREEMENT BETWEEN TWO METHODS OF CLINICAL MEASUREMENT,” The Lancet, **327**(8476), pp. 307–310.